



Using field observations to inform thermal hydrology models

A. L. Atchley et al.

Using field observations to inform thermal hydrology models of permafrost dynamics with ATS (v0.83)

A. L. Atchley¹, S. L. Painter², D. R. Harp¹, E. T. Coon¹, C. J. Wilson¹, A. K. Liljedahl^{3,4}, and V. E. Romanovsky⁵

¹Earth and Environmental Sciences Division, Los Alamos National Laboratory, Los Alamos, NM, USA

²Climate Change Science Institute, Environmental Sciences Division, Oak Ridge National Laboratory, Oak Ridge, TN, USA

³Water and Environmental Research Center, Univ. of Alaska Fairbanks, USA

⁴International Arctic Research Center, Univ. of Alaska Fairbanks, USA

⁵Geophysical Institute, Univ. of Alaska Fairbanks, USA

Received: 24 January 2015 – Accepted: 12 March 2015 – Published: 14 April 2015

Correspondence to: A. L. Atchley (aatchley@lanl.gov)

Published by Copernicus Publications on behalf of the European Geosciences Union.

Title Page

Abstract

Introduction

Conclusions

References

Tables

Figures



Back

Close

Full Screen / Esc

Printer-friendly Version

Interactive Discussion



Abstract

Climate change is profoundly transforming the carbon-rich Arctic tundra landscape, potentially moving it from a carbon sink to a carbon source by increasing the thickness of soil that thaws on a seasonal basis. However, the modeling capability and precise parameterizations of the physical characteristics needed to estimate projected active layer thickness (ALT) are limited in Earth System Models (ESMs). In particular, discrepancies in spatial scale between field measurements and Earth System Models challenge validation and parameterization of hydrothermal models. A recently developed surface/subsurface model for permafrost thermal hydrology, the Advanced Terrestrial Simulator (ATS), is used in combination with field measurements to calibrate and identify fine scale controls of ALT in ice wedge polygon tundra in Barrow, Alaska. An iterative model refinement procedure that cycles between borehole temperature and snow cover measurements and simulations functions to evaluate and parameterize different model processes necessary to simulate freeze/thaw processes and ALT formation. After model refinement and calibration, reasonable matches between simulated and measured soil temperatures are obtained, with the largest errors occurring during early summer above ice wedges (e.g. troughs). The results suggest that properly constructed and calibrated one-dimensional thermal hydrology models have the potential to provide reasonable representation of the subsurface thermal response and can be used to infer model input parameters and process representations. The models for soil thermal conductivity and snow distribution were found to be the most sensitive process representations. However, information on lateral flow and snowpack evolution might be needed to constrain model representations of surface hydrology and snow depth.

Using field observations to inform thermal hydrology models

A. L. Atchley et al.

Title Page

Abstract

Introduction

Conclusions

References

Tables

Figures



Back

Close

Full Screen / Esc

Printer-friendly Version

Interactive Discussion



1 Introduction

In Arctic tundra, the thickness of the soil layer that reaches above 0°C temperatures, defined as the active layer thickness (ALT), largely determines the volume of carbon stores available for decomposition. Predicting ALT is therefore critical when characterizing potential climate feedbacks due to greenhouse gas release into the atmosphere from decomposition of organic soil carbon (McGuire et al., 2009; Koven et al., 2011; Schneider von Deimling et al., 2012). Current long-term predictions of ALT generally use large-scale Earth System Models (ESMs) with simplified representations of the hydrothermal processes, and are thus producing results with significant uncertainty (Schaefer et al., 2009; Slater and Lawrence, 2013; Koven et al., 2014). The freeze–thaw dynamics that determine the ALT function on a vertical scale of centimeters and vary horizontally on a scale of meters across the characteristic microtopography of polygonal tundra (Painter et al., 2013). Freeze–thaw dynamics are also strongly controlled by local inundation state (Muster et al., 2012), which can vary over a horizontal extent of meters to hundreds of meters. These local-to-intermediate scale processes are under-resolved or completely missing in ESMs. Therefore, improved fine-scale simulation capabilities can inform the representation of soil thermal processes in regional to global scale models.

Previous efforts have been made to characterize ALT using field, lab, and numerical experiments (e.g. Osterkamp and Romanovsky, 1996; Romanovsky and Osterkamp, 1997). Site-specific properties of Arctic soils, such as porosity, bulk thermal conductivity, and water retention characteristics have been measured in lab settings from samples taken in the field (Hinzman et al., 1991; Letts et al., 2010). Those field and lab measured properties were then used in ESMs in order to predict future ALT and permafrost conditions (Beringer et al., 2001; Lawrence and Slater, 2008; Subin et al., 2013). However, such regional and global scale projections are difficult to constrain by measurements of soil properties made at vastly smaller scales of observation. This scale-gap between the governing fine-scale physical processes and large-scale sim-

GMDD

8, 3235–3292, 2015

Using field observations to inform thermal hydrology models

A. L. Atchley et al.

Title Page

Abstract

Introduction

Conclusions

References

Tables

Figures



Back

Close

Full Screen / Esc

Printer-friendly Version

Interactive Discussion



Using field observations to inform thermal hydrology models

A. L. Atchley et al.

Title Page

Abstract

Introduction

Conclusions

References

Tables

Figures



Back

Close

Full Screen / Esc

Printer-friendly Version

Interactive Discussion



ulations impedes direct model validation against measurements, which has motivated development of fine to intermediate-scale hydrothermal models (e.g. Hinzman et al., 1998; Hansson et al., 2004; Daanen et al., 2007; McKenzie et al., 2007; Painter 2011; Karra et al., 2014; Endrizzi et al., 2014). Numerical experiments using high-resolution coupled hydrothermal models, which are calibrated against fine-scale measurements, can play a fundamental role in understanding the governing physical processes of ALT formation.

Simulating thermal hydrology in polygonal tundra systems is a challenging endeavor that requires simultaneous representation of multiple physical processes including phase change and highly nonlinear constitutive relationships (e.g. Painter, 2011). Soil thermal conductivity alone depends on volumetric water content, mineral composition, porosity, density, and temperature (Farouki, 1981). In soils experiencing freeze–thaw cycles, the phase of water also affects bulk thermal conduction (e.g. Johansen, 1977; Peters-Lidard et al., 1997). Latent heat of fusion and evaporation impart further control on the propagation of the freezing front and therefore thermal conduction. Thermally driven vapor transport can slowly change ice content and thus thermal conduction in partially and fully frozen soils (Grimm and Painter, 2009; Karra et al., 2014). Characterizing subsurface properties for modeling is further complicated due to variability in microtopography and cryoturbated soil that create a heterogeneous surface and subsurface in polygonal tundra systems. In addition, coupling of the soil to the atmosphere involves a balance among multiple energy transfer processes, which occur across interfaces of snow, water, ice and exposed ground. All of the above attributes describing soil structure, surface energy balances, and processes of phase change result in a tightly coupled hydrothermal system. Therefore, numerical experiments using high-fidelity representations of fine-scale processes require calibrated parameters that are able to effectively link dependent processes.

Despite the model gains of calibrating thermal properties (Romanovsky and Osterkamp, 1997; Nicolsky et al., 2009), relatively few hydrothermal modeling studies of Arctic systems have documented calibration procedures, with the noted exception of

hydrological parameters for moss, peat, and mineral soil layers, along with a consistent model structure, employed for various microtopographic positions characteristic of polygonal tundra. We demonstrate how the detailed calibration and model development effort informs understanding of the key processes that define the ALT in polygonal ground. We further complete the ModEx cycle by discussing how future data needs can reduce system uncertainty and refine our understanding of process behavior.

2 Methods

2.1 ModEx process applied to thermal hydrology processes in permafrost

Our variant of the ModEx approach is shown schematically in Fig. 2. Starting with site identification and characterization, field observations and measurements begin to form the modeling activity by providing model parameter inputs and targets for the model calibration process. Standard model calibration – denoted by the inner loop – aims to match simulations to field measurements by varying parameters while keeping the model structure fixed. Here the ModEx procedure moves beyond the standard calibration by assuming the model itself is unknown, but can be refined through successive comparison to observation (outer loop in Fig. 2). These improved model runs then inform the observation process by specifying the data needs, either through informal numerical experimentation or through more formal data worth exercises. Such model refinement is not a unique process, and can be achieved through multiple avenues. We implement ModEx model refinement by focusing on the plausibility of calibrated parameters in addition to the mismatch between field measurements and simulated responses.

The calibration process uses a multi-dimensional response surface to evaluate the plausibility of parameters and the degree of mismatch between simulated results and observed data. Sets of parameters values are mapped to the response surface with the respective mismatch between simulated results and field observations/measurements,

Using field observations to inform thermal hydrology models

A. L. Atchley et al.

Title Page

Abstract

Introduction

Conclusions

References

Tables

Figures



Back

Close

Full Screen / Esc

Printer-friendly Version

Interactive Discussion



quantified by the root-mean-squared error (RMSE), which determines the shape of the responses surface. RMSE is given by:

$$\text{RMSE} = \sqrt{\frac{1}{N} \sum_{i=1}^N (\hat{T}_i(\theta) - T_i)^2} \quad (1)$$

where θ is a vector comprised of a combination of parameter values, $\hat{T}_i(\theta)$ is the i th simulated temperature given θ , and T_i is the i th calibration measured temperature target, and N is the number of calibration targets. Simulations with a poor fit to data have high RMSE and a corresponding high value on the response surface. Conversely simulations with a good fit to data have a low RMSE and therefore a low value on the response surface and may constitute a minimum in the response surface. A minimum in the response surface indicates that a possible calibration has been achieved. However, in the case of a complex model with high dimensionality, multiple local minima may exist, which results in gradient-based calibrations finding many solutions to the problem (Beven, 2006). Model structure error can also cause the response surface to slope to a parameter boundary indicating that over-fitting is necessary to calibrate to observed data (Beven, 2005). It is important to extend calibration boundaries beyond the acceptable parameter range in order to both diagnose model inadequacy and avoid boundary effects caused by automated calibration algorithms. By altering the model itself, and not just model parameters the ModEx process can work to reduce model structure error and reshape the response surface such that the simulated system matches the observed data and calibrated parameters are realistic.

The ModEx process is facilitated by two software components. First, for calibrating a given model to determine an optimal match to the measurements we use PEST (Doherty, 2004), which implements the Levenberg–Marquardt algorithm (Marquardt, 1963). This method uses gradient descent to determine (from a high-dimensional space of calibration parameters) a set of parameters that (in a local sense) minimize the forward model's error in predicting observed data. Second, the ModEx process requires itera-

GMDD

8, 3235–3292, 2015

Using field observations to inform thermal hydrology models

A. L. Atchley et al.

Title Page

Abstract

Introduction

Conclusions

References

Tables

Figures

⏪

⏩

◀

▶

Back

Close

Full Screen / Esc

Printer-friendly Version

Interactive Discussion



ary of parameter space. Together the eight starting calibration parameter sets determined the dependence of calibration results on starting location (i.e. the degree of non-uniqueness in the calibration results).

3 Subsurface ModEx results

3.1 ModEx applied to the subsurface system

Our experience with the ModEx cycle applied to the coupled subsurface hydrothermal system at the BEO is shown in process flow form in Fig. 4. In this cycle the ATS model only included subsurface processes, and the shallowest measurement of temperature (2 cm depth) was used as a time-dependent upper boundary condition to force the model. Measurements at deeper locations (from 0.1 to 1.5 m) (Fig. 3) represented the calibration targets. In the initial iteration, calibration was performed using the BPC model for thermal conductivity and assumed full saturation of the soil column. That calibration resulted in parameters being out of range. In the second iteration, the thermal conductivity model was changed to an alternative model (the MC model), which resulted in improved parameter values but inferior match to measured soil temperatures. In the final iteration, surface pressure was calibrated at the borehole locations, which determines liquid saturation that affects near surface thermal conductivity. The iteration to calibrate surface pressure resulted in a calibration that was judged to be adequate for continuation of a coupled surface energy balance–subsurface calibration and model development (see Sect. 4). Details of the subsurface calibration and model development are discussed in the remainder of this section.

3.2 Subsurface BPC vs. MC thermal model

The first subsurface calibration attempt used the BPC model (Fig. 4) and resulted in unrealistic parameters sets. The response surface of the center and rim columns resulted in calibrated peat porosities to move to the lower parameter boundary (Fig. 5).

Using field observations to inform thermal hydrology models

A. L. Atchley et al.

Title Page

Abstract

Introduction

Conclusions

References

Tables

Figures



Back

Close

Full Screen / Esc

Printer-friendly Version

Interactive Discussion



bration, where surface pressures were calibrated, also resulted in realistic parameters with surface pressures at 95440.9 and 97638.2 Pa for the center and trough respectively (Table 5). Moreover, the revised coupled calibration found a low RMSE of 0.554 °C and the temperature time-series results fit measured data near the point of the active layer depth (Fig. 7).

4 Coupled surface/subsurface model

4.1 Surface methods

After the calibration of subsurface thermal properties, a 2 cm moss layer was added to each of the three columns and a surface energy balance model was used to calibrate both the thermal properties of the moss layer and parameter values for the surface energy balance in a second set of ModEx iterations (Fig. 8). Parameters from the subsurface calibration were used in the coupled snow-surface energy balance–subsurface simulation. The ranges of hydrothermal parameters for moss are listed in Table 1. The surface energy balance, described in detail in Appendix B, is implicitly coupled with subsurface thermal hydrology and is based on the work of Hinzman et al. (1998) and Ling and Zhang (2004). Simulated snow deformation and snow density changes described by Eqs. (B6) and (B7) in Appendix B on a single layered of snowpack. The center, rim, trough columns had unique maximum head boundary conditions of 8, 0.7, and 15 cm respectively, were water spills off each column at or above the specified head heights. The maximum head boundary conditions were selected according to relative elevation differences observed in polygonal tundra.

For the surface energy balance calibration each column was spun-up over a 10 year loop using decadal averaged air temperature along with shortwave radiation, relative humidity, and windspeed data from 1 October 1998 to 30 September 2009 at Barrow, AK, where meteorological data from each day in the ten years was averaged together. After spin-up, daily meteorological data from 2010–2013 were used to drive the model.

Using field observations to inform thermal hydrology models

A. L. Atchley et al.

Title Page

Abstract

Introduction

Conclusions

References

Tables

Figures



Back

Close

Full Screen / Esc

Printer-friendly Version

Interactive Discussion



Using field observations to inform thermal hydrology models

A. L. Atchley et al.

Title Page

Abstract

Introduction

Conclusions

References

Tables

Figures



Back

Close

Full Screen / Esc

Printer-friendly Version

Interactive Discussion



near the observed ALT range. However, near-surface winter rim temperatures were colder than measured because microtopography-informed snow distribution produces less snow on rims and results in less snow cover insulation. The third iteration of the ModEx cycle added a depth hoar representation in the snowpack, which resulted in a better representation of winter rim soil temperatures and caused the rim ALT to be within the range of observed ALT. In the final ModEx iteration hydrothermal properties of moss and surface energy balance parameters were hand calibrated within the plausible range of parameters space, which resulted in only slight improvements of near surface temperature simulations. Details of how each iteration of the ModEx cycle (for the coupled surface energy balance–subsurface model) informed both model development and future data needs are presented below.

4.3 Importance of surface energy balance governing saturation time series

Forcing the subsurface thermal propagation through a surface energy balance in the second set of ModEx cycles attempts to capture variable surface thermal conductivities due to changing surface saturation states as pulses of precipitation enter the subsurface and subsequently dry from evaporation. Modeling studies that do not explicitly model surface energy balance processes may not adequately capture near-surface saturation states and have reported the greatest error during the summer when highly variable soil moisture states occur (Romanovsky and Osterkamp, 1997; Jiang et al., 2012). It is known that soil moisture influences soil temperature in addition to meteorological controls, by governing the amount of latent heat of fusion necessary to freeze/thaw and evaporate water from soils (Johansen, 1977; Farouki, 1981; Peters-Lidard et al., 1998; Subin et al., 2013). Consequently, the timing of the precipitation pulses and subsequent drying may have a significant impact on ALT because the highly variable saturation states coincide with summer soil warming. Therefore, the second set of ModEx cycles starts with a more detailed representation of transient soil moisture conditions, which is the third major model refinement. Simulation results showed that it is important to capture the freeze-up timing with the highly variable fall saturation

state in order to set up near surface ice content and thermal conductivity during winter (Fig. 1, plot A). Properly representing the freeze-up with transient soil moisture is especially important giving that winter has the largest range of possible thermal conductivity values (Fig. 6) and therefore is highly variable from year to year.

5 Simulating the surface energy balance for each column resulted in varied model fits to the measured 2 cm soil temperature time series. For example, the simulated center and trough 2 cm soil temperature during the summer is consistently lower than the measured 2 cm temperature (Fig. 9, center and trough plots), especially for the early summer, which in turn lowers the simulated soil temperature at depth. However, simulated
10 simulated 2 cm deep soil temperatures for the rim matched measured soil temperatures. The ability for the model to match measured summer surface temperatures for the rim vs. the center and trough is most likely attributed to either the spatial differences and local microtopography of the three columns and/or the surface saturation state. The rim is higher and therefore drier than the center and trough columns (Fig. 3). To mimic micro-
15 topographical differences in the three columns, unique maximum ponded water depths were assigned to each column, the rim had a negligible max ponded depth with effectively no standing water from snow melt compared to the center and trough columns. Unfortunately, limitations to our surrogate 1-D model exist and inherently contribute to model structural error. For example, the largest deviation of surface temperature for
20 the trough occurred during the fall as the temperature dropped below freezing. The measured surface temperature at 2 cm depth had a longer duration of the zero curtail, where soil temperatures are at 0°C as water freezes, compared to the simulated surface temperature (Fig. 9). One possible explanation for this difference is that there is greater soil moisture in the trough than was simulated, as added soil moisture will extend the time to freeze a block of soil. A possible reason for the underestimated soil
25 moisture is that the 1-D surrogate model neglected lateral surface- and subsurface flow that could be flowing on to the column, especially for troughs that are connected to an extensive trough-network. Monitoring of lateral flow in polygonal tundra systems could help to constrain the conceptual model needed to understand soil moisture dynamics.

Using field observations to inform thermal hydrology models

A. L. Atchley et al.

[Title Page](#)[Abstract](#)[Introduction](#)[Conclusions](#)[References](#)[Tables](#)[Figures](#)[Back](#)[Close](#)[Full Screen / Esc](#)[Printer-friendly Version](#)[Interactive Discussion](#)

4.4 Snow model refinement

The largest gains from calibrating the surface energy balance portion of the model came from the fourth model refinement, which resulted from two additional ModEx iterations (1) updating the conceptual and numerical model to add snow depth variation informed by microtopography and (2) include a depth hoar representation in the snowpack model. The snowpack at Barrow, AK is scoured relatively flat due to strong winds (Benson and Sturm, 1993; Zhang et al., 1996) resulting in deeper snow in depressions such as troughs and low-centers. To match measured snow depths of the three topographical features (Table 3), snowfall was increased for the center and trough columns by 30 (3.6 cm) and 82.5% (9.9 cm), respectively, and reduced for the rim to 87% (10.4 cm) of the total adjusted snowfall (12 cm) for the snow year of 2012–2013. Although manually distributing snow does not fully capture snowpack dynamics, especially year-to-year snowpack variation, simulated near surface (2 cm) winter temperature more accurately matched the measured temperatures (Fig. 9, center and trough plots). Summer ALT increased for both the center and trough, which improved the model prediction to be within the observed ALT range for the trough and closer to the observed ALT range for the center column (Table 4). Conversely, the decreased snow depth over the rim cooled the winter surface soil temperature below the measured soil temperatures. Including a depth hoar layer in the model counteracted the reduced insulation of a shallower snowpack on the rim. The combination of reduced snow depth and depth hoar representation on the rim translated to a slightly shallower ALT, resulting in the rim ALT to be within the observed ALT range.

Without snow re-distribution or depth hoar representation the snowpack evolved to a density of 410 to 440 kg m⁻³ by mid May and early June as determined from Eq. (B26). At first, this seemed reasonable because the surface of tundra snow forms a wind slab layer due to the wind scouring affect with densities between 400–500 kg m⁻³ (Benson and Sturm, 1993; Dominé et al., 2002). Having a snowpack surface with high densities is required to accurately capture snow surface albedo. How-

GMDD

8, 3235–3292, 2015

Using field observations to inform thermal hydrology models

A. L. Atchley et al.

Title Page

Abstract

Introduction

Conclusions

References

Tables

Figures

⏪

⏩

◀

▶

Back

Close

Full Screen / Esc

Printer-friendly Version

Interactive Discussion



Using field observations to inform thermal hydrology models

A. L. Atchley et al.

Title Page

Abstract

Introduction

Conclusions

References

Tables

Figures



Back

Close

Full Screen / Esc

Printer-friendly Version

Interactive Discussion



ever, underneath the wind slab layer, a hoar layer forms during the winter with a density between $100\text{--}250\text{ kg m}^{-3}$, (Benson and Sturm, 1993; Zhang et al., 1996; Zhang, 2005), which reduces the thermal conductivity of the snowpack. The single layer snow model did not include the formation of a depth hoar layer and would overestimate the thermal conduction of the snowpack and therefore, increase winter cooling of the ground surface. The iterative ModEx process however, encouraged us to formulate a way of both representing snowpack top densities in order to properly simulate surface albedo, and capture a depth hoar layer to account for lower snowpack thermal conduction. The new formulation, similar to the snow classes used by Schaefer et al. (2009) and Sturm et al. (1995), employed in the model runs plotted in Fig. 9, calculates a new thermal conduction by assuming a depth hoar layer forms for 15 % of the snowpack with a calibrated density. Then a harmonic mean snow density is taken between the depth hoar layer and rest of the snowpack in order to calculate an adjusted thermal conductivity of the snowpack. Because this process applies only to calculating the snowpack thermal conduction, the simulation of snow albedo is unaffected. Center and Rim depth hoar densities calibrated to 110 kg m^{-3} and the trough depth hoar density calibrated to 190 kg m^{-3} . The addition of the depth hoar also reduced end of winter (2 May) snowpack densities from above 400 to between 320 to 370 kg m^{-3} (Table 3), which is closer to the measured end-of-winter average snowpack density of 326 kg m^{-3} .

Adjusting the snow accumulation due to topographically informed snow distribution and including a depth hoar representation increased the insulative effect of the snowpack and had a clear impact on winter near surface temperatures (Fig. 9). In addition snow distribution and depth hoar representation improved summertime ALT predictions (Table 4). Summertime changes in ALT due to winter conditions highlights a memory trait of the system and the necessity to capture dominant winter processes in order to simulate transient thermal conditions in physically based models. Research by Hinkel and Hurd (2006) showed that large snow drifts cause long term deepening of the ALT, due in part from the additional insulation for the snow and the loss of cold thermal propagation into the subsurface. Timing of snowpack accumulation and thickness has

Using field observations to inform thermal hydrology models

A. L. Atchley et al.

[Title Page](#)

[Abstract](#)

[Introduction](#)

[Conclusions](#)

[References](#)

[Tables](#)

[Figures](#)



[Back](#)

[Close](#)

[Full Screen / Esc](#)

[Printer-friendly Version](#)

[Interactive Discussion](#)



also been shown to govern permafrost formation (Zhang, 2005). However at the scale of microtopographical relief, where trough to rim vertical relief changes by 40 cm within a horizontal distance of a meter, questions regarding how snow thickness and associated melt water inputs affect ALT formation remain. Results for this work show that topographically informed snow distribution will change the spring and early summer surface saturation state (Fig. 10, plot D) due to distributed snow water equivalence amounts (Table 3). The change in early summer surface saturation state then affects the thermal conduction for early summer as well as adding greater water mass that then requires a greater amount of energy to heat up (Hinkel and Hurd, 2006). Moreover, studies have found that the depth hoar layer can be as thick as 50 % of the snowpack height in arctic conditions (Sturm et al., 1995; Schaefer et al., 2009). However, due to continuous wind slab and depth hoar formation significant snowpack heterogeneities develop within and across topographical features (Sturm and Benson, 2004; Sturm et al., 2004). Therefore, spatially distributed snow depth measurements and snowpack density profiles that characterize local snowpack variability and over microtopographical features can help constrain both modeled snowpack thermal conduction representation, and surface water inputs.

4.5 Surface energy balance calibration

In the final ModEx iteration and model refinement, attempts to increase the simulated summer surface (2 cm) temperature were made (Fig. 8). Special attention was paid to the early summer wet conditions found in the center and trough for the Julian dates between 150 and 200 (Fig. 10, plots B and D), where the biggest error in surface temperatures is found (Fig. 9 center and rim plots). It was thought that by calibrating parameters which control the amount of energy entering the subsurface under wet conditions, such as the albedo of standing water (see Appendix B for details), the surface temperature of the center and trough, which are wet, will increase without affecting the relatively dry rim surface temperature. However, variables specific to the surface energy balance and moss properties had little effect of simulated soil temperature during

Using field observations to inform thermal hydrology models

A. L. Atchley et al.

Title Page

Abstract

Introduction

Conclusions

References

Tables

Figures

◀

▶

◀

▶

Back

Close

Full Screen / Esc

Printer-friendly Version

Interactive Discussion



the snow free summer. The range of accepted albedo values for tundra varied from 0.12 to 0.17 based on wet or dry conditions (Grenfell and Perovich, 2004), and the albedo range for standing water values ranged from 0.11–0.20 for the months of May through September for latitude of 70° near Barrow, AK (Cogley, 1979). Only slight gains in simulated surface temperature were observed by decreasing albedo of standing water from 0.14 to 0.11 and tundra from 0.15 to 0.12. This iteration of the ModEx cycle shows that adjusted standing water albedo and roughness length within the perceived parameter range did not substantially improve model fit, which suggest that the model is lacking either a necessary process representation or the calibration parameter range is not correct. One possible improvement would be a distributed surface albedo representation that provides a unique albedo for centers, rims, and troughs. Local-scale tundra albedo measurements can inform models of spatially distributed albedo conditions. Another possible explanation is how atmospheric mixing coefficients such as roughness length (noted as z in Eq. B12 in Appendix B) could change over microtopographical features. Specific exchange coefficients for each microtopographical feature would then produce unique sensible and latent heat fluxes. For example, rim surface temperatures were well matched under current roughness lengths. But topographically protected troughs and centers could have a different roughness length, which may result in changes to latent and sensible heat exchanges and higher surface temperatures. Observations of how microtopography affect near surface wind and associated atmospheric mixing could support an improved conceptualization of sensible and latent heat exchanges.

5 Summary and conclusions

1-D thermal hydrology models of transient saturation and frozen states combined with a surface energy balance model were used to represent active layer dynamics in polygonal tundra at the Barrow Environmental Observatory. In the coupled model, surface water was allowed to pond to a specified maximum height but any additional water

Using field observations to inform thermal hydrology models

A. L. Atchley et al.

Title Page

Abstract

Introduction

Conclusions

References

Tables

Figures



Back

Close

Full Screen / Esc

Printer-friendly Version

Interactive Discussion



was removed (spill over condition). The surface model also includes a surface energy balance model for bare, snow-, ice- or water-covered ground. The model was used in combination with borehole temperature and snowpack field measurements in an iterative model–data integration (ModEx) framework to produce calibrated model parameters and refine constitutive models and process representations. The particular variant of the ModEx approach combined calibration with iterative refinement of the model structure; parameter feasibility and model–observation mismatch were used as metrics in the model refinement process.

The results demonstrate the effectiveness of using borehole temperature measurements to effectively develop and refine the model structure for hydrothermal models of permafrost-affected landscapes. Results also suggest that properly constructed and calibrated 1-D models coupled to a surface energy balance may be adequate for representing thermal response at a given location provided the maximum ponded depth (spill point) is known for that location. This suggests a multiscale modeling strategy that uses overland flow models to establish the spill point (maximum ponded depth) at each surface location in conjunction with a set of thermal hydrology simulations. Further evaluations of the 1-D representations against 3-D model representations are needed, however. In addition, it is important to note that the largest discrepancy between model and field measurements occurred during early summer in the troughs and that mismatch is likely indicating model structural error with inflow of water from upstream locations and/or unique surface energy balance conditions. Observations of water fluxes such as evapotranspiration, lateral flow, and snowmelt at the sub-polygon scale would help model representation, and in particular, role of advective lateral heat transport. However, the temperature mismatch was brief and confined to the trough location, and is thus not expected to have large consequences for integrated results such as thaw depth.

The model refinement process identified the representation of thermal conductivity – specifically the dependence of bulk thermal conductivity on porosity, water content, and ice content – as a constitutive model that affects model performance. Thus, field

and laboratory work to better constrain hydrothermal representation and the governing model parameters would help reduce uncertainty in model projections. Similarly, snowpack properties and snow distribution were found to be important. Investigations similar to Benson and Sturm (1993), Zhang et al. (1996) and Tape et al. (2010) that better define the relationship between depth hoar, microtopography and wind slab formation would help reduce uncertainty in projections. For example, snowpack dynamics and density profile observations at the NGEA-Arctic site will inform models of how the snowpack develops and how snow will distribute across microtopography.

More generally, these results demonstrated the utility of one particular approach to merging observations and models in environmental applications. In this particular iterative approach, formal parameter estimation methods are used iteratively. Each calibration run – the inner loop in Fig. 2 – minimizes mismatch between data and model with fixed model structure. The “reasonableness” or feasibility of the calibrated parameters and the RMSE are performance metrics for the calibrated model. Model structural adjustment, the outer loop in Fig. 2, is initiated when calibrated parameters fall outside reasonable bounds. Although structural model adjustments were done in an ad-hoc manner guided by experience and knowledge of the system being modeled, the resulting refinements have produced robust representation of system response. Such an approach combining structural model adjustments drawing from literature, field observations and formal calibration exercises is likely to be useful in other environmental applications.

6 Code availability

The Advance Terrestrial Simulator (version 0.83) is a suite of physics modules managed within the Arcos metaphysics framework that couples multiple model components at run-time. ATS, Arcos, and the host software AMANZI is developed by Los Alamos National Labs and the source code is available upon request (eoon@lanl.gov), interested parties should see <http://software.lanl.gov/ats> for more information. The input

Using field observations to inform thermal hydrology models

A. L. Atchley et al.

Title Page

Abstract

Introduction

Conclusions

References

Tables

Figures



Back

Close

Full Screen / Esc

Printer-friendly Version

Interactive Discussion



data and calibration results presented here can be obtained by contacting the lead author via e-mail, or accessed at the NGE-E-Arctic data portal: doi:10.5440/1167674.

Appendix A: Thermal conductivity model

Farouki (1981) reviewed methods for calculating the thermal conductivity of soils and concluded that a modification to a method by Johansen (1977) was superior to other models in most conditions. Peters-Lidard et al. (1998) provide a clear summary of the modified Johansen approach. Following Painter (2011), we further modify the approach to a form convenient for a three-phase model and to more accurately represent thermal conductivity of peat and organic-rich soils.

Thermal conductivity in unfrozen soils is often written as (Johansen, 1977; Farouki, 1981; Peters-Lidard, 1998)

$$\kappa_e = \kappa_{\text{dry}} + (\kappa_{\text{sat,l}} - \kappa_{\text{dry}}) \text{Ke}_u \quad (\text{A1})$$

where $\text{Ke}_u(s_l)$ is the Kersten number (Kersten, 1949) for unfrozen conditions, s_l is the liquid saturation index, $\kappa_{\text{sat,l}}$ is the liquid-saturated thermal conductivity and κ_{dry} is the dry conductivity.

For soils that are frozen and with no liquid water content, the corresponding equation is

$$\kappa_e = \kappa_{\text{dry}} + (\kappa_{\text{sat,i}} - \kappa_{\text{dry}}) \text{Ke}_f \quad (\text{A2})$$

where $\text{Ke}_f(s_i)$ is the Kersten number for frozen conditions, s_i is the ice saturation, $\kappa_{\text{sat,i}}$ is the thermal conductivity under ice-saturated conditions.

For a general-purpose three-phase code, thermal conductivity is needed as a function of both s_l and s_i . To this end, bilinear interpolation in the Kersten numbers may be used (Painter, 2011)

$$\kappa_e = \text{Ke}_f \kappa_{\text{sat,f}} - \text{Ke}_u \kappa_{\text{sat,u}} + (1 - \text{Ke}_f - \text{Ke}_u) \kappa_{\text{dry}} \quad (\text{A3})$$

3258

Using field observations to inform thermal hydrology models

A. L. Atchley et al.

Title Page

Abstract

Introduction

Conclusions

References

Tables

Figures

◀

▶

◀

▶

Back

Close

Full Screen / Esc

Printer-friendly Version

Interactive Discussion



The Kersten numbers in Eqs. (A1) and (A2) are simply ratios of partially saturated thermal conductivity to fully saturated thermal conductivity. Both range from 0 for dry conditions to 1 for saturated conditions and are, in general, nonlinear functions of the respective saturation indices.

5 A variety of empirical fits have been used to relate the Kersten numbers to saturation indices for ice and liquid (see, e.g. Farouki, 1981 for a summary). A simple power-law function is assumed here as a convenient model (Painter, 2011)

$$\text{Ke}_u = (s_l + \varepsilon)^{\alpha_u} \quad (\text{A4})$$

$$\text{Ke}_f = (s_l + \varepsilon)^{\alpha_f} \quad (\text{A5})$$

10 where α_u and α_f are empirical exponents and $\varepsilon \ll 1$ is a regularization parameter that prevents, for numerical reasons, the derivative with respect to s_l or s_i from becoming unbounded at 0 when α_u and α_f are less than 1.

For saturated conductivity, geometric means are often used (Johansen, 1977)

$$K_{\text{sat},u} = K_s^{1-\phi} K_w^\phi \quad (\text{A6})$$

15 and

$$K_{\text{sat},f} = K_s^{1-\phi} K_i^\phi \quad (\text{A7})$$

where K_i , K_w , K_s are thermal conductivities for water ice, liquid water, and soil solids, respectively. We take $K_{\text{sat},u}$ as a property of the medium which can be measured or calibrated, then assume

$$20 K_{\text{sat},f} = K_{\text{sat},uf} \left(\frac{K_i}{K_w} \right)^\phi \quad (\text{A8})$$

consistent with Eqs. (A6) and (A7).

We denote the model specified by Eqs. (A3), (A4), (A5) and (A8) with input parameters, $K_{\text{sat},uf}$, K_{dry} , α_u , and α_f as the BPC model.

Using field observations to inform thermal hydrology models

A. L. Atchley et al.

Title Page

Abstract

Introduction

Conclusions

References

Tables

Figures

⏪

⏩

◀

▶

Back

Close

Full Screen / Esc

Printer-friendly Version

Interactive Discussion



An alternative model, which we denote the MC model, is obtained by relating κ_{dry} and $\kappa_{\text{sat,uf}}$ to the thermal conductivities of the material components (ice, liquid, gas, and soil solids). For κ_{dry} the following empirical fit has been suggested (Johansen, 1977)

$$\kappa_{\text{dry}} = \frac{0.135\rho_b + 64.7}{\rho_s - 0.947\rho_b} \quad (\text{A9})$$

where ρ_b and ρ_s are the dry bulk and solid densities, respectively, in kg m^{-3} and κ_{dry} is in $\text{W m}^{-1} \text{K}^{-1}$. Using $\rho_b = \rho_s(1 - \phi)$, this equation can be placed in the form

$$\kappa_{\text{dry}} = \frac{0.135\rho_s(1 - \phi) + 64.7}{\rho_s - (1 - d)\rho_s(1 - \phi)} = \frac{0.135(1 - \phi) + 64.7/\rho_s}{\phi + d(1 - \phi)} \quad (\text{A10})$$

where d is 0.053 (unitless). Equation (9) is problematic as a general model for two reasons. First, the thermal conductivity of air should be recovered as porosity approaches unity, which is not the case in Eq. (9). Second, the thermal conductivity of the soil solids should be recovered when the porosity is zero, which is also not the case for Eq. (9). Setting porosity to 0 results in a thermal conductivity of $\sim 3 \text{W m}^{-1} \text{K}^{-1}$ for soil minerals with grain density of 2700kg m^{-3} , which is consistent with a “typical” value (van Wijk, 1963) of $2.9 \text{W m}^{-1} \text{K}^{-1}$ at $\rho_s = 2700 \text{kg m}^{-3}$. However, setting ρ_s to the value of a typical organic material (1.3kg m^{-3}) results in $\sim 3.5 \text{W m}^{-1} \text{K}^{-1}$, which is more than an order of magnitude greater than a typical value for peat ($0.25 \text{W m}^{-1} \text{K}^{-1}$).

To better represent κ_{dry} for organic-rich soils, we thus modify Eq. (9) to be

$$\kappa_{\text{dry}} = \frac{d(1 - \phi)\kappa_s + \kappa_a\phi}{d(1 - \phi) + \phi} \quad (\text{A11})$$

where κ_a is the thermal conductivity of air and κ_s is the thermal conductivity of soil solids. When porosity is 0, $\kappa_{\text{dry}} = \kappa_s$ is recovered from Eq. (A11). When porosity is 1, $\kappa_{\text{dry}} = \kappa_a$. A comparison between Eq. (A11) and the Johansen equivalent (Eq. A9) for

Using field observations to inform thermal hydrology models

A. L. Atchley et al.

Title Page

Abstract

Introduction

Conclusions

References

Tables

Figures

⏪

⏩

◀

▶

Back

Close

Full Screen / Esc

Printer-friendly Version

Interactive Discussion



Using field observations to inform thermal hydrology models

A. L. Atchley et al.

Title Page

Abstract

Introduction

Conclusions

References

Tables

Figures

⏪

⏩

◀

▶

Back

Close

Full Screen / Esc

Printer-friendly Version

Interactive Discussion



a mineral soil ($\rho_s = 2700 \text{ kg m}^{-3}$ in Eq. (A9) and $\kappa_s = 2.9 \text{ W m}^{-1} \text{ K}^{-1}$ in Eq. A11). The Johansen fit and our modification (Eq. A11) have only very minor differences in this case. However, for peat material ($\rho_s = 1300 \text{ kg m}^{-3}$ in Eq. A9 and $\kappa_s = 0.25 \text{ W m}^{-1} \text{ K}^{-1}$ in Eq. A10), the two models diverge. The alternative parameterization of using κ_s instead of ρ_s in Eq. (A11) provides enough flexibility to produce reasonable values for dry thermal conductivity for both mineral soil and peat.

In summary, two thermal conductivity models are available. The BPC model uses the following parameters: thermal conductivity of dry soil, saturated thermal conductivity in unfrozen conditions, the exponents α_u and α_{uf} , and porosity. The MC model uses the following parameters: thermal conductivity of soil solid, the exponents α_u and α_{uf} , and porosity. Although each of these may be determined by laboratory measurements on core samples, the use of such small-scale measurements at the field scale is often confounded by multiscale heterogeneity. We thus use field-scale temperature measurements to estimate the parameters.

Appendix B: Snow-surface-energy-balance model

The surface energy balance model is a coupled mass and energy balance simulator used to deliver energy fluxes and any water associated with snowmelt or precipitation to the ground surface simulated by the Advanced Terrestrial Simulator (ATS). The surface energy simulator is split into two parts depending on if snow is present or absent. If snow is present, the surface energy balance solves the snow surface temperature (T_s) following the methods by Hinzman et al. (1998) and Ling and Zhang (2004). Energy fluxes are then delivered through a mass conservative evolving snowpack deformation model to the surface of the ground. In addition to energy, water mass is also delivered to ground surface. The surface energy balance equation for snow is:

$$0 = (1 - \alpha)Q_{\text{sw, met}}^{\text{In}} + Q_{\text{lw}}^{\text{In}} + Q_{\text{lw}}^{\text{Out}}(T_s) + Q_{\text{h}}(T_s) + Q_{\text{e}}(T_s) + Q_{\text{c}}(T_s) \quad (\text{B1})$$

Q_{lw}^{in} and $Q_{sw, met}^{in}$ are incoming long and shortwave radiation respectively, Q_{lw}^{out} is outgoing long-wave radiation. Q_h is sensible heat, Q_e is latent heat, and Q_c is the conduction of heat from the snow surface through the snowpack to the ground surface. All energy balance components are in $[W m^{-2}]$. This method assumes the snowpack is in equilibrium with all energy fluxes going into and out of the snowpack. If no snow is present, the energy balance is calculated on the top of the surface water, bare tundra, or a gradation between the two, and the water and energy fluxes are delivered to the subsurface portion of ATS. The ground surface energy balance equation without snow is:

$$Q_{gf} = (1 - \alpha)Q_{sw}^{in} + Q_{lw}^{in} + Q_{lw}^{out}(T_{gs}) + Q_h(T_{gs}) + Q_e(T_{gs}) \quad (B2)$$

T_{gs} is the ground surface temperature and Q_{gf} is the flux of energy into the subsurface and because no snow is present, Q_c is no longer computed.

Components of the energy balance model that do not depend on the surface temperature are computed initially, Q_{lw}^{in} and $Q_{sw, met}^{in}$. Q_{lw}^{in} can be either read in from a data file or modeled based on an empirical equation for calculating the emissivity of air from Satterlund (1979):

$$Q_{lw}^{in} = \varepsilon_a \sigma T_a^4 \quad (B3)$$

where σ is the Stephan–Boltzmann Constant, $5.670676 \times 10^{-8} [W m^{-2} K^{-4}]$, and T_a is the air temperature [K]. The emissivity of air (ε_a) is calculated by:

$$\varepsilon_a = 1.08 \left(1 - \exp^{-(0.01 e_a)^{\frac{T_a}{2016}}} \right). \quad (B4)$$

where e_a is the vapor pressure of air.

Q_{sw}^{in} in the surface energy balance model is the shortwave radiation absorbed by the surface, after a percentage of the total shortwave radiation from the meteorological

Using field observations to inform thermal hydrology models

A. L. Atchley et al.

Title Page

Abstract

Introduction

Conclusions

References

Tables

Figures



Back

Close

Full Screen / Esc

Printer-friendly Version

Interactive Discussion



data ($Q_{sw, met}^{In}$) has been reflected by the albedo (α) of the surface.

$$Q_{sw}^{In} = (1 - \alpha)Q_{sw, met}^{In} \quad (B5)$$

The albedo α in Barrow, Alaska can change spatially due to heterogeneous surface conditions and temporally due to the changing physical conditions of the surface (Grenfell and Perovich, 2004). The changing surface conditions between snow, ice, and water strongly influence incoming shortwave radiation by altering α ; therefore its representation in the model plays a critical role in accurately simulating the arctic energy budget (Curry et al., 1995; Hansen and Nazarenko, 2004). Currently, there are four possible surfaces with unique α values (1) snow, (2) ice, (3) ponded water, and (4) tundra vegetation.

The α of snow is based on snow density (ρ_s) following the methods of Anderson (1976), Ling and Zhang (2004), and Peter ReVelle's thesis (2012) and reflects the aging process of snow deformation.

if $\rho_s \leq 450 \text{ kg m}^{-3}$

$$\alpha = 1 - 0.247 \left(0.16 + 110 \left(\frac{\rho_s}{1000} \right)^4 \right)^{0.5} \quad (B6)$$

if $\rho_s > 450 \text{ kg m}^{-3}$

$$\alpha = 0.6 - \frac{\rho_s}{4600} \quad (B7)$$

The snow deformation model is outlined in Martinec (1977).

The albedo of the four possible surfaces are listed in Table (B1).

The α of ponded water is the average α of standing water at a latitude of 70° from May through September. During freezing and thawing of the ground surface any ponded water is subdivided into an unfrozen water fraction and a frozen water fraction in ATS. The α values for this surface is then an average of water and ice α values and

Using field observations to inform thermal hydrology models

A. L. Atchley et al.

Title Page	
Abstract	Introduction
Conclusions	References
Tables	Figures
◀	▶
◀	▶
Back	Close
Full Screen / Esc	
Printer-friendly Version	
Interactive Discussion	



are found to transition linearly between the two states (Grenfell and Perovich, 2004) based on unfrozen water fraction. Transitional α values between each type of surface can occur and are triggered when the snowpack height is less than 2 cm, or the standing water height is less than 10 cm. The transition height for ponded water is based on the penetration depth of shortwave radiation in ice (10 cm). Transitional α weighting values are calculated by:

$$\begin{aligned} \text{Tran}_{\text{snow}} &= \left(\frac{Z_s}{\text{Pen}_s} \right)^2 \\ \text{Tran}_{\text{water}} &= \frac{Z_w}{\text{Pen}_w} [1 - \text{Tran}_{\text{snow}}] \\ \text{Tran}_{\text{tundra}} &= [1 - \text{Tran}_{\text{snow}}] - \text{Tran}_{\text{water}} \end{aligned} \quad (\text{B8})$$

where Z is the height of water or snow and Pen is the penetration depth of shortwave radiation. The transitional α value is then calculated by:

$$\alpha_{\text{trans}} = \alpha_{\text{snow}} \text{Tran}_{\text{snow}} + \alpha_{\text{water}} \text{Tran}_{\text{water}} + \alpha_{\text{tundra}} \text{Tran}_{\text{tundra}} \quad (\text{B9})$$

In this model, if snow is present it is always the top surface, and ponded water or surface ice will always be below snow and above the tundra surface. Therefore, the α value is set first by snow, if present, then by standing water and/or ice if present, and finally by the tundra surface.

Once the incoming radiation components of the energy balance model are computed, evaporative resistance (E_r) is then calculated by:

$$E_r = \frac{1}{R_{\text{air}} + R_{\text{soil}}} \quad (\text{B10})$$

Using field observations to inform thermal hydrology models

A. L. Atchley et al.

Title Page

Abstract

Introduction

Conclusions

References

Tables

Figures

⏪

⏩

◀

▶

Back

Close

Full Screen / Esc

Printer-friendly Version

Interactive Discussion



where the air resistance term (R_{air}) is the inverse of the turbulent exchange of latent and sensible heat (D_{eh}) and the stability function (ζ):

$$R_{\text{air}} = \frac{1}{D_{\text{eh}}\zeta} \quad (\text{B11})$$

$$D_{\text{eh}} = \frac{\kappa^2 U_s}{(\ln(z_r/z_0))^2} \quad (\text{B12})$$

5 κ is the von Karman Constant 0.41 [–], U_s is the wind speed at the reference height (z_r) of the meteorological measurement location. z is the roughness length. Due to the changing conditions of the landscape at barrow, z changes from 0.005 [m] for wind swept snow (Wieringa and Rudel, 2002), to 0.04 [m] for polygonal tundra (Weller and Holmgren, 1974; Hansen, 1993).

10 The stability function (ζ) accounts for both stable (ζ_{stable}) and unstable (ζ_{unstable}) atmospheric conditions (Price and Dunne, 1976)

$$\zeta_{\text{stable}} = \frac{1}{1 + 10R_i} \text{ or } \zeta_{\text{unstable}} = 1 - 10R_i. \quad (\text{B13})$$

15 ζ_{unstable} conditions occur when the ground surface (T_s) is warmer than the air temperature (T_a) causing more air to mix vertically. R_i defines atmospheric stability; where R_i is positive in the stable condition and R_i is negative in an unstable condition.

$$R_i = \frac{gz_r(T_a - T_s)}{T_a U_s^2} \quad (\text{B14})$$

20 g is the acceleration due to gravity. R_{soil} [ms^{-1}] is calculated following the methods used by Sakaguchi and Zeng (2009) and is only implemented during ground surface evaporation when the saturation state of the upper most subsurface cell adjacent to the domain surface is less than 1.

$$R_{\text{soil}} = \frac{L}{D} \quad (\text{B15})$$

Using field observations to inform thermal hydrology models

A. L. Atchley et al.

Title Page

Abstract

Introduction

Conclusions

References

Tables

Figures

⏪

⏩

◀

▶

Back

Close

Full Screen / Esc

Printer-friendly Version

Interactive Discussion



where D is vapor diffusion [$\text{m}^2 \text{s}^{-1}$] calculated empirically (Moldrup et al., 2004; Sakaguchi and Zeng, 2009) from the residual saturation (θ_r), saturation (θ_{sat}), and the molecular diffusion coefficient of water vapor in the air (D_o), assumed to be constant 2.2×10^{-5} [$\text{m}^2 \text{s}^{-1}$] (Moldrup et al., 1999; Sakaguchi and Zeng, 2009).

$$D = D_o \theta_{\text{sat}}^2 \left(1 - \frac{\theta_r}{\theta_{\text{sat}}}\right)^{2+3b} \quad (\text{B16})$$

The exponent b in Eq. (B16) is a Clapp and Hornberger (1978) fitting parameter for the soil water characteristic curve, assumed to be 1 for moss (Beringer et al., 2001), which covers the tundra surface and is simulated as the top subsurface layer for the tundra.

L is dry layer thickness or the length vapor must travel from the point of evaporation.

$$L = d_1 \frac{\exp\left[(1 - \theta_l/\theta_{\text{sat}})^w\right] - 1}{e - 1} \quad (\text{B17})$$

Once all necessary components of the energy balance are calculated, either the snow energy balance or surface energy balance is computed. The snow energy balance, Eq. (B1), is calculated if snow height (Z_s) is more than 2 cm. The ground surface energy balance, Eq. (B2), is used if no snow is present. Between Z_s of 0 and 2 cm, a transition between the snow energy balance and the ground surface energy balance is used where both conditions are solved. When calculating the energy balance for the transitional regime, the snow energy balance assumes a Z_s of 2 cm for all components that depend on Z_s and an area-weighted average is used between the ground surface and snow energy balance based on the actual Z_s that is equal to or less than 2 cm. Assuming a 2 cm Z_s within the snow energy balance calculation prevents unreasonable heat conduction through the snowpack (Q_c), calculated by:

$$Q_c = -\frac{k_s (T_s - T_g)}{Z_s} \quad (\text{B18})$$

Using field observations to inform thermal hydrology models

A. L. Atchley et al.

Title Page

Abstract

Introduction

Conclusions

References

Tables

Figures

◀

▶

◀

▶

Back

Close

Full Screen / Esc

Printer-friendly Version

Interactive Discussion



where k_s is the effective thermal conductivity of snow [$\text{Wm}^{-1}\text{K}^{-1}$] and is calculated from an empirical function of ρ_s used by Ling and Zhang, (2004), described by Goodrich (1982)

$$k_s = 2.9 \times 10^{-6} \rho_s^2. \quad (\text{B19})$$

5 The snow and surface energy balance use the same formulation for Q_h and Q_{lw}^{Out} . Q_h is:

$$Q_h = \rho_a C_p D_{eh} \zeta (T_a - T_s) \quad (\text{B20})$$

where ρ_a is the density of air $1.275 [\text{kgm}^{-3}]$, and C_p is the specific heat of air ($1004 \text{JK}^{-1} \text{kg}^{-1}$). Q_{lw}^{Out} is:

$$10 \quad Q_{lw}^{\text{Out}} = -\varepsilon_s \sigma T_s^4 \quad (\text{B21})$$

ε_s is the emissivity of the surface. The ε_s for snow and ice 0.98 [-], is taken from Liston and Hall, (1995), and the ε_s for tundra is 0.92 (Ling and Zhang, 2004) and for standing water is 0.979 (Robinson and Davis, 1972).

15 Q_e is slightly different between the snow and ground surface energy balance where the porosity (ϕ_s) of the top cell in the ground surface is included for the surface energy balance calculation.

$$Q_{e, \text{snow}} = \rho_a L_s E_r \left(0.622 \frac{e_a - e_s}{A_{pa}} \right)$$

$$Q_{e, \text{ground_surface}} = \phi_s \rho_a L_s E_r \left(0.622 \frac{e_a - e_s}{A_{pa}} \right) \quad (\text{B22})$$

20 where E_r , the evaporation resistance as defined by Eq. (B8) and R_{soil} is 0 in the case of snow, or condensation on the surface. L_s is the latent heat of sublimation

for snow ($2834000 \text{ J kg}^{-1}$) and L_e is the latent heat of evaporation for the ground surface ($2497848 \text{ J kg}^{-1}$). e_s is the vapor pressure of the snow or surface, and A_{pa} is the atmospheric pressure (101.325 kPa).

Once the energy balance is calculated, then the water fluxes to the ground surface are calculated. In the case of snow, if the snow surface temperature (T_s) is greater than freezing, T_s is set to freezing and the snow surface energy balance is recalculated with all excess energy assigned to the melting energy (Q_m), and a melting rate (Mr) [m s^{-1}] is calculated from:

$$\text{Mr} = \frac{Q_m}{\rho_w \times H_f}, \quad (\text{B23})$$

where ρ_w is the density of water and H_f is the heat of fusion for melting snow $333500 \text{ [J kg}^{-1}\text{]}$. Condensation or sublimation of the snow surface is also calculated from Q_e , where the sublimation/condensation rate (S_r) is added to the total water flux. If T_a and $Z_s > 0$ and S_r is positive, then

$$Q_{\text{water}} = S_r + P_r$$

$$S_r = \frac{Q_e}{\rho_w L_s}, \quad (\text{B24})$$

Sublimation is removed from the snowpack when S_r is positive. If only the surface energy balance is used then water is delivered to the ground surface as precipitation and condensation when S_r is negative. Water is evaporated from the surface/sub-surface when S_r is positive.

Snow water equivalence (SWE), Z_s , and ρ_s are tracked through the simulation of snowpack evolution and related by:

$$\text{SWE} = \frac{Z_s}{\rho_s}, \quad (\text{B25})$$

Using field observations to inform thermal hydrology models

A. L. Atchley et al.

Title Page	
Abstract	Introduction
Conclusions	References
Tables	Figures
◀	▶
◀	▶
Back	Close
Full Screen / Esc	
Printer-friendly Version	
Interactive Discussion	



Both Z_s and ρ_s are important in the snow energy balance equation for calculated Q_c and snow α , and both variables evolve as the snowpack ages through snowpack deformation simulated by (Martinec, 1977):

$$\rho_{\text{settled}} = \rho_{\text{freshsnow}}(\text{SP}_{\text{age}})^{0.3} \quad (\text{B26})$$

5 where $\rho_{\text{freshsnow}}$ is assigned a density of 100 kg m^{-3} , SP_{age} is the age of the snowpack. The total snowpack density and Z_s are then calculated by a weighted average of 3 components: old settled snow, new snow accumulation, and any ice from condensation. The density of condensation is assigned 200 kg m^{-3} .

Appendix C: Parameter literature sources

10 Values for hydrothermal properties of moss were gathered from Hinzman et al. (1991); Letts et al. (2000); Quinton et al. (2000); Price et al. (2008); O'Donnell et al. (2009); and Zhang et al. (2010). Large-scale simulations including a moss layer were also considered and informed valid parameters ranges (Beringer et al., 2001). Peat properties were found in Hinzman et al. (1991, 1998); Letts et al. (2000); Quinton et al. (2000, 15 2008); Nicolisky et al. (2009); Zhang et al. (2010) and the accompanying larger scale simulations (Beringer et al., 2001; Lawrence and Slater, 2008). Mineral soil properties were gathered from Hinzman et al. (1991, 1998); Beringer et al. (2001); Overduin et al. (2006); Lawrence and Slater, (2008); Nicolisky et al. (2009). van Genuchten parameters were fitted to the published soil water characteristics curves (Hinzman et al., 1991).

20 **The Supplement related to this article is available online at doi:10.5194/gmdd-8-3235-2015-supplement.**

Acknowledgements. This work was supported by the Los Alamos National Laboratory, Laboratory Direction Research and Development project LDRD201200068DR and by the Next Generation Ecosystem Experiment (NGEE-Arctic) project. NGEE-Arctic is supported by the Office of Biological and Environmental Research in the DOE Office of Science. We are also dearly

indebted to all field personal, in particular Andy Chamberlain, William Cable, and Robert Busey, who braved freezing temperatures, polar bears, and mosquito swarms to provide the necessary field measurements to develop our models.

References

- 5 Anderson, E. A.: A point energy and mass balance model of a snow cover, NOAA Tech. Rep. NWS-19, Office of Hydrology National Weather Service Silver Spring, Md., 1976.
- Atmospheric Radiation Measurement (ARM) Climate Research Facility: updated hourly. Surface Meteorological Instrumentation (MET). 2010-01-01 to 2013-12-31, 71.323 N 156.609 W: North Slope Alaska (NSA) Central Facility, Barrow AK (C1), compiled by: Kyrouac, J. and Holdridge, D., Atmospheric Radiation Measurement (ARM) Climate Research Facility Data Archive, Oak Ridge, Tennessee, USA, data set accessed 19 May 2014 at doi:10.5439/1025220, 1993.
- 10 Atmospheric Radiation Measurement (ARM) Climate Research Facility: updated hourly. Sky Radiometers on Stand for Downwelling Radiation (SKYRAD60S). 2010-01-01 to 2013-12-31, 71.323 N 156.609 W: North Slope Alaska (NSA) Central Facility, Barrow AK (C1), compiled by: Morris, V., Sengupta, M., Habte, A., Reda, I., Anderberg, M., Dooraghi, M., Gotseff, P., Morris, V., Andreas, A., and Kutchenreiter, M., Atmospheric Radiation Measurement (ARM) Climate Research Facility Data Archive, Oak Ridge, Tennessee, USA, data set accessed 19 May 2014 at doi:10.5439/1025281, 1996.
- 15 Benson, C. S. and Sturm, M.: Structure and wind transport of seasonal snow on the Arctic slope of Alaska, *Ann. Glaciol.*, 18, 261–267, 1993.
- Beringer, J., Lynch, A. H., Chapin III, F. S., Mack, M., and Bonan, G. B.: The representation of Arctic soils in the Land Surface Model: the importance of Mosses, *J. Climate*, 14, 3324–3335, 2001.
- 20 Beven, K.: On the concept of model structural error, *Water Sci. Technol.*, 52, 167–175, 2005.
- Beven, K.: A manifesto for the equifinality thesis, *J. Hydrol.*, 320, 18–36, doi:10.1016/j.jhydrol.2005.07.007, 2006.
- Clapp, R. B. and Hornberger, G. M.: Empirical equations for some soil hydraulic properties, *Water Resour. Res.*, 14, 601–604, doi:10.1029/WR014i004p00601, 1978.

Using field observations to inform thermal hydrology models

A. L. Atchley et al.

Title Page

Abstract

Introduction

Conclusions

References

Tables

Figures



Back

Close

Full Screen / Esc

Printer-friendly Version

Interactive Discussion



Using field observations to inform thermal hydrology models

A. L. Atchley et al.

Title Page

Abstract

Introduction

Conclusions

References

Tables

Figures



Back

Close

Full Screen / Esc

Printer-friendly Version

Interactive Discussion



- Cogley, J. G.: The albedo of water as a function of latitude, *Mon. Weather Rev.*, 107, 775–781, 1979.
- Coon, E. T., Moulton, J. D., Berndt, M., Manzini, G., Garimella, R., Lipnikov, K., and Painter, S. L.: Coupled surface and subsurface hydrologic flow using mimetic finite differences, *Adv. Water Resour.*, in review, 2015a.
- Coon, E. T., Moulton, J. D., and Painter, S. L.: Managing complexity in simulations of land surface and near-surface processes, *Environ. Modell. Softw.*, in review, 2015b.
- Curry, J. A., Schramm, J. L., and Ebert, E. E.: Sea ice–albedo climate feedback mechanism, *J. Climate*, 8, 240–247, 1995.
- Daanen, R. P., Misra, D., and Epstein, H.: Active-layer hydrology in nonsorted circle ecosystems of the arctic tundra, *Vadose Zone J.*, 6, 694–704, 2007.
- Doherty, J.: PEST Model-Independent Parameter Estimation User Manual, Watermark Numerical Computing, Brisbane, Australia, 2004.
- Dominé, F., Cabanes, A., and Legagneux, L.: Structure, microphysics, and surface area of the Arctic snowpack near Alert during the ALERT 2000 campaign, *Atmos. Environ.*, 36, 2753–2765, 2002.
- Endrizzi, S., Gruber, S., Dall'Amico, M., and Rigon, R.: GEOtop 2.0: simulating the combined energy and water balance at and below the land surface accounting for soil freezing, snow cover and terrain effects, *Geosci. Model Dev.*, 7, 2831–2857, doi:10.5194/gmd-7-2831-2014, 2014.
- Farouki, O. T.: The thermal properties of soils in cold regions, *Cold Reg. Sci. Technol.*, 5, 67–75, 1981.
- Grenfell, T. C. and Perovich, D. K.: Seasonal and spatial evolution of albedo in a snow-ice-land-ocean environment, *J. Geophys. Res.*, 109, C01001, doi:10.1029/2003JC001866, 2004.
- Grimm, R. E. and Painter, S. L.: On the secular evolution of groundwater on Mars, *Geophys. Res. Lett.*, 36, doi:10.1029/2009GL041018, 2009.
- Goodrich, L. E.: The influence of snow cover on the ground thermal regime, *Can. Geotech. J.*, 19, 421–432, 1982.
- Gupta, J. V., Clark, M. P., Vrugt, J. A., Abramowitz, G., and Ye, M.: Towards a comprehensive assessment of model structural adequacy, *Water Resources Research.*, 48, W08301, doi:10.1029/2011WR011044, 2012.
- Hansen, S. V.: Surface roughness lengths. ARL Technical Report US Army, White Sands Missile Range, White Sands Missile Range, NM 55002-5501, 1993.

Using field observations to inform thermal hydrology models

A. L. Atchley et al.

[Title Page](#)[Abstract](#)[Introduction](#)[Conclusions](#)[References](#)[Tables](#)[Figures](#)[Back](#)[Close](#)[Full Screen / Esc](#)[Printer-friendly Version](#)[Interactive Discussion](#)

- Hansen, J. and Nazarenko, L.: Soot climate forcing via snow and ice albedos, *Proceedings of the National Academy of Sciences of the United States of America*, 101, 423–428, 2004.
- Hansson, K., Šimůnek, J., Mizoguchi, M., Lundin, L. C., and Van Genuchten, M. T.: Water flow and heat transport in frozen soil, *Vadose Zone Journal*, 3, 693–704, 2004.
- 5 Hinkel, K. M. and Hurd Jr., J. K.: Permafrost destabilization and thermokarst following snow fence installation, Barrow, Alaska, USA, *Arct. Antarct. Alp. Res.*, 38, 530–539, 2006.
- Hinzman, L. D., Kane, D. L., Gieck, R. E., and Everett, K. R.: Hydrological and thermal properties of the active layer in the Alaskan Arctic, *Cold Reg. Sci. Technol.*, 19, 95–110, 1991.
- 10 Hinzman, L. D., Goering, D. J., and Kane, D. L.: A distributed thermal model for calculating soil temperature profiles and depth of thaw in permafrost regions, *J. Geophys. Res.*, 103, 28975–28991, 1998.
- Jiang, Y., Zhuang, Q., and O'Donnell, J. A.: Modeling thermal dynamics of active layer soils and near-surface permafrost using a fully coupled water and heat transport model, *J. Geophys. Res.*, 117, D1110, doi:10.1029/2012JD017512, 2012.
- 15 Johansen, O.: Thermal conductivity of soils (No. CRREL-TL-637), Cold Regions Research and Engineering Lab, Hanover, NH, 1977.
- Karra, S., Painter, S. L., and Lichtner, P. C.: Three-phase numerical model for subsurface hydrology in permafrost-affected regions (PFLOTTRAN-ICE v1.0), *The Cryosphere*, 8, 1935–1950, doi:10.5194/tc-8-1935-2014, 2014.
- 20 Kersten, M. S.: Thermal Properties of Soils, University of Minnesota, Institute of Technology, Engineering Experiment Station, Bulletin 28, University of Minnesota, Institute of Technology, Engineering Experiment Station, Bulletin 28, 1949.
- Koven, C. D., Ringeval, B., Friedlingstein, P., Ciais, P., Cadule, P., Khvorostyanov, D., Krinner, G., and Tarnocai, C.: Permafrost carbon-climate feedbacks accelerate global warming, *P. Natl. Acad. Sci. USA*, 108, 14769–14774, doi:10.1073/pnas.1103910108, 2011.
- 25 Larsen, L., Thomas, C., and Eppinga, M.: Exploratory modeling: extracting causality from complexity, *EOS*, 95, 285–292, 2014.
- Lawrence, D. M. and Slater, A. G.: Incorporating organic soil into a global climate model, *Clim. Dynam.*, 30, 145–160, doi:10.1007/s00382-007-0278-1, 2008.
- 30 Letts, M. G., Roulet, N. T., Comer, N. T., Skarupa, M. R., and Verseghy, D. L.: Parameterization of peatland hydraulic properties for the Canadian land surface scheme, *Atmos. Ocean*, 38, 141–160, 2000.

Using field observations to inform thermal hydrology models

A. L. Atchley et al.

Title Page

Abstract

Introduction

Conclusions

References

Tables

Figures



Back

Close

Full Screen / Esc

Printer-friendly Version

Interactive Discussion



- Liljedahl, A. K., Hinzman, L. D., Harazono, Y., Zona, D., Tweedie, C. E., Hollister, R. D., Engstrom, R., and Oechel, W. C.: Nonlinear controls on evapotranspiration in arctic coastal wetlands, *Biogeosciences*, 8, 3375–3389, doi:10.5194/bg-8-3375-2011, 2011.
- Ling, F. and Zhang, T.: A numerical model for surface energy balance and thermal regime of the active layer and permafrost containing unfrozen water, *Cold Reg. Sci. Technol.*, 38, 1–15, doi:10.1016/S0165-232X(03)00057-0, 2004.
- Liston, G. E. and Hall, D. K.: An energy balance model of lake ice evolution, *J. Glaciol.*, 41, 373–382, 1995.
- Marquardt, D. W.: An algorithm for least-squares estimation of nonlinear parameters, *J. Soc. Ind. Appl. Math.*, 11, 431–441, 1963.
- Martinec, J.: Expected snow loads on structures from incomplete hydrological data, *J. Glaciol.*, 19, 185–195, 1977.
- McGuire, A. D., Anderson, L. G., Christensen, T. R., Dallimore, S., Guo, L., Hayes, D. J., and Roulet, N.: Sensitivity of the carbon cycle in the Arctic to climate change, *Ecol. Monogr.*, 79, 523–555, 2009.
- McKenzie, J. M., Voss, C. I., and Siegel, D. I.: Groundwater flow with energy transport and water–ice phase change: numerical simulations, benchmarks, and application to freezing in peat bogs, *Adv. Water Resour.*, 30, 966–983, 2007.
- Moldrup, P., Olesen, T., Yamaguchi, T., Schjønning, P., and Rolston, D. E.: Modeling diffusion and reaction in soils: IX. The Buckingham–Burdine–Campbell equation for gas diffusivity in undisturbed soil, *Soil Sci.*, 164, 542–551, 1999.
- Moldrup, P., Olesen, T., Yoshikawa, S., Komatsu, T., and Rolston, D. E.: Three-porosity model for predicting the gas diffusion coefficient in undisturbed soil, *Soil Sci. Soc. Am. J.*, 68, 750–759, 2004.
- Muster, S., Langer, M., Heim, B., Westermann, S., and Boike, J.: Subpixel heterogeneity of ice-wedge polygonal tundra: a multi-scale analysis of land cover and evapotranspiration in the Lena River Delta, Siberia, *Tellus B*, 64, 17301, doi:10.3402/tellusb.v64i0.17301, 2012.
- Nicolosky, D. J., Romanovsky, V. E., Alexeev, V. A., and Lawrence, D. M.: Improved modeling of permafrost dynamics in a GCM land-surface scheme, *Geophys. Res. Lett.*, 34, L08501, doi:10.1029/2007GL029525, 2007.
- Nicolosky, D. J., Romanovsky, V. E., and Panteleev, G. G.: Estimation of soil thermal properties using in-situ temperature measurements in the active layer and permafrost, *Cold Reg. Sci. Technol.*, 55, 120–129, 2009.

Using field observations to inform thermal hydrology models

A. L. Atchley et al.

Title Page

Abstract

Introduction

Conclusions

References

Tables

Figures



Back

Close

Full Screen / Esc

Printer-friendly Version

Interactive Discussion



- Osterkamp, T. E. and Romanovsky, V. E.: Characteristics of changing permafrost temperatures in the Alaskan Arctic, USA, *Arctic Alpine Res.*, 28, 267–273, 1996.
- Overduin, P. P., Kane, D. L., and van Loon, W. K. P.: Measuring thermal conductivity in freezing and thawing soil using the soil temperature response to heating, *Cold Reg. Sci. Technol.*, 45, 8–22, doi:10.1016/j.coldregions.2005.12.003, 2006.
- Painter, S. L.: Three-phase numerical model of water migration in partially frozen geological media: model formulation, validation, and applications, *Comput. Geosci.*, 15, 69–85, doi:10.1007/s10596-010-9197-z, 2011.
- Painter, S. L. and Karra, S.: Constitutive model for unfrozen water content in subfreezing unsaturated soils, *Vadose Zone J.*, 13.4, doi:10.2136/vzj2013.04.0071, 2014.
- Painter, S. L., Moulton, J. D., and Wilson, C. J.: Modeling challenges for predicting hydrologic response to degrading permafrost, *Hydrogeol. J.*, 21, 221–224, doi:10.1007/s10040-012-0917-4, 2013.
- Peters-Lidard, C. D., Blackburn, E., Liang, X., and Wood, E. F.: The effect of thermal conductivity parameterization on surface energy fluxes and temperatures, *J. Atmosphere*, 55, 1209–1224, 1998.
- Price, A. D. and Dunne, T.: Energy balance computations of snow melt in a sub-Arctic area, *Water Resour. Res.*, 12, 686–689, 1976.
- Price, J. S., Elrick, D. E., Strack, M., Brunet, N., and Faux, E.: A method to determine unsaturated hydraulic conductivity in living and undecomposed *Sphagnum* moss, *Soil Sci. Soc. Am. J.*, 72, 487–491, doi:10.2136/sssaj2007.0111N, 2008.
- Quinton, W. L., Gray, D. M., and Marsh, P.: Subsurface drainage from hummock-covered hillslopes in the Arctic tundra, *J. Hydrol.*, 237, 113–125, 2000.
- Quinton, W. L., Hayashi, M., Carey, S. K., and Myers, T.: Peat hydraulic conductivity in cold regions and its relation to pore size and geometry, *Hydrol. Process.*, 22, 2829–2837, 2008.
- ReVelle, P.: A Snow Model Used to Examine the Affect of Seasonal Snow on an Arctic Environment, New Mexico Tech, Department of Earth and Environmental Science, 2012.
- Robinson, P. J. and Davies, J. A.: Laboratory determination of water surface emissivity, *J. Appl. Meteorol.*, 11, 1391–1393, 1972.
- Romanovsky, V. E. and Osterkamp, T. E.: Thawing of the active layer on the coastal plain of the Alaskan Arctic, *Permafrost Periglac.*, 8, 1–22, 1997.
- Romanovsky, V. and Osterkamp, T.: Effects of unfrozen water on heat and mass transport processes in the active layer and permafrost, *Permafrost Periglac.*, 11, 219–239, 2000.

Using field observations to inform thermal hydrology models

A. L. Atchley et al.

Title Page

Abstract

Introduction

Conclusions

References

Tables

Figures



Back

Close

Full Screen / Esc

Printer-friendly Version

Interactive Discussion



- Sakaguchi, K. and Zeng, X.: Effects of soil wetness, plant litter, and under-canopy atmospheric stability on ground evaporation in the Community Land Model (CLM3.5), *J. Geophys. Res.*, 114, D01107, doi:10.1029/2008JD010834, 2009.
- Satterlund, D. R.: An improved equation for estimating long-wave radiation from the atmosphere, *Water Resour. Res.*, 15, 1649–1650, 1979.
- Schaefer, K., Zhang, T., Slater, A. G., Lu, L., Etringer, A., and Baker, I.: Improving simulated soil temperatures and soil freeze/thaw at high-latitude regions in the Simple Biosphere/Carnegie-Ames-Stanford Approach model, *J. Geophys. Res.-Earth*, 114, F02021, 2009.
- Schneider von Deimling, T., Meinshausen, M., Levermann, A., Huber, V., Frieler, K., Lawrence, D. M., and Brovkin, V.: Estimating the near-surface permafrost-carbon feedback on global warming, *Biogeosciences*, 9, 649–665, doi:10.5194/bg-9-649-2012, 2012.
- Shiklomanov, N. I., Nelson, F. E., and Streletskiy, D. A.: The Circumpolar Active Layer Monitoring (CALM) Program: data collection, management, and dissemination strategies, in: Tenth International Conference on Permafrost Vol. 1: International Contributions, edited by: Hinkel, K. M., The Northern Publisher, Salekhard, Russia, 377–382, 25–29 June, 2012.
- Sturm, M. and Benson, C.: Scales of spatial heterogeneity for perennial and seasonal snow layers, *Ann. Glaciol.*, 38, 253–260, 2004.
- Sturm, M., Holmgren, J., and Liston, G. E.: A seasonal snow cover classification system for local to global applications, *J. Climate*, 8, 1261–1283, 1995.
- Sturm, M., Johnson, J. B., and Holmgren, J.: Variations in the mechanical properties of arctic and subarctic snow at local (1-m) to regional (100-km) scales, in: Proceedings ISSMA-2004, International Symposium on Snow Monitoring and Avalanches, 25–29 June 2012, Manali, India, vol. 12, p. 16, 2004.
- Subin, Z. M., Koven, C. D., Riley, W. J., Torn, M. S., Lawrence, D. M., and Swenson, S. C.: Effects of soil moisture on the responses of soil temperature to climate change in cold regions, *J. Climate*, 26, 3139–3158, doi:10.1175/JCLI-D-12-00305.1, 2013.
- Tang, J. and Zhuang, Q.: Modeling soil thermal and hydrological dynamics and changes of growing season in Alaskan terrestrial ecosystems, *Climatic Change*, 107, 481–510, 2011.
- Tape, K. D., Rutter, N., Marshall, H. P., Essery, R., and Sturm, M.: Recording microscale variations in snowpack layering using near-infrared photography, *J. Glaciol.*, 56, 75–80, 2010.
- Van Wijk, W. R.: *Physics of Plant Environment*, Amsterdam: North Holland Publishing, 1963.
- Watanabe, K. and Wake, T.: Measurement of unfrozen water content and relative permittivity of frozen unsaturated soil using NMR and TDR, *Cold Reg. Sci. Technol.*, 59, 34–41, 2009.

Using field observations to inform thermal hydrology models

A. L. Atchley et al.

Title Page

Abstract

Introduction

Conclusions

References

Tables

Figures

⏪

⏩

◀

▶

Back

Close

Full Screen / Esc

Printer-friendly Version

Interactive Discussion



Weller, G. and Holmgren, B.: The microclimates of the arctic tundra, *J. Appl. Meteorol.*, 13, 854–862, 1974.

Wieringa, J. and Rudel, E.: Station exposure metadata needed for judging and improving quality of observations of wind, temperature and other parameters. Paper 2.2 in WMO Technical Conference on Meteorological and Environmental Instruments and Methods of Observation (TECO-2002), 23 September–3 October 2002, Bratislava, Slovak Republic, 2002.

Yang, D., Goodison, B. E., Ishida, S., and Benson, C.: Adjustment of daily precipitation data of 10 climate stations in Alaska: applications of world meteorological organization intercomparison results, *Water Resour. Res.*, 34, 241–256, 1998.

Zhang, T.: Influence of the seasonal snow cover on the ground thermal regime: an overview, *Rev. Geophys.*, 43, RG4002, doi:10.1029/2004RG000157, 2005.

Zhang, T., Osterkamp, T. E., and Stamnes, K.: Influence of the depth hoar layer of the seasonal snow cover on the ground thermal regime, *Water Resour. Res.*, 32, 2075–2086, 1996.

Zhang, Y., Carey, S. K., Quinton, W. L., Janowicz, J. R., Pomeroy, J. W., and Flerchinger, G. N.: Comparison of algorithms and parameterisations for infiltration into organic-covered permafrost soils, *Hydrol. Earth Syst. Sci.*, 14, 729–750, doi:10.5194/hess-14-729-2010, 2010.

Zona, D., Lipson, D. A., Richards, J. H., Phoenix, G. K., Liljedahl, A. K., Ueyama, M., Sturtevant, C. S., and Oechel, W. C.: Delayed responses of an Arctic ecosystem to an extreme summer: impacts on net ecosystem exchange and vegetation functioning, *Biogeosciences*, 11, 5877–5888, doi:10.5194/bg-11-5877-2014, 2014.

Using field observations to inform thermal hydrology models

A. L. Atchley et al.

Table 1. Valid parameter range for calibration sets.

Notation/units	Moss-Range	Peat-Range	Mineral-Range
Porosity [-]	0.88–0.95	0.7–0.93	0.2–0.75
VG Alpha [1 Pa^{-1}]	1×10^{-5} – 2.35×10^{-3}	3.1×10^{-7} – 1.2×10^{-3}	2.9×10^{-4} – 1×10^{-3}
VG n [-]	1.3–2.82	1.3–1.9	0.1–0.33
Residual VWC [-]	0.02–0.18	0.04–0.22	0.05–0.18
$K_{\text{dry,Bulk}}$ [$\text{W m}^{-1} \text{ K}^{-1}$]	0.007–0.3	0.05–0.38	0.2–1.6
$K_{\text{unfrozen,Bulk Sat}}$ [$\text{W m}^{-1} \text{ K}^{-1}$]	0.5–0.59	0.43–2.9	0.96–3.1
$K_{\text{frozen,Bulk Sat}}$ [$\text{W m}^{-1} \text{ K}^{-1}$]	0.81–2.8	0.81–2.3	1.31–2.8
$K_{\text{dry,material}}$ [$\text{W m}^{-1} \text{ K}^{-1}$]	0.022–0.20	0.05–0.38	0.2–4.0
$\alpha_{\text{T,uf}}$ [-]	–	–	–
$\alpha_{\text{T,f}}$ [-]	–	–	–

^a $K_{\text{dry,material}}$ [$\text{W m}^{-1} \text{ K}^{-1}$] is back calculated from $K_{\text{dry,Bulk}}$.

Title Page

Abstract

Introduction

Conclusions

References

Tables

Figures

⏪

⏩

◀

▶

Back

Close

Full Screen / Esc

Printer-friendly Version

Interactive Discussion



Using field observations to inform thermal hydrology models

A. L. Atchley et al.

Title Page

Abstract

Introduction

Conclusions

References

Tables

Figures

◀

▶

◀

▶

Back

Close

Full Screen / Esc

Printer-friendly Version

Interactive Discussion



Table 2. The calibration error from the measured values reported as the RMSE °C (ϕ) increased between the (1) BPC model to the (2) MC saturated model. Thus there was greater error in the model results, but the calibrated parameters were more realistic. ϕ then decreased between the (2) MC saturated model and (3) the MC unsaturated model.

Calibration Start	BPC			MC			MC – Freed Pressure	
	Center	Trough	Rim	Center	Trough	Rim	Center	Trough
1	0.461	0.616	0.642	0.646	0.834	0.831	0.503	0.781
2	0.444	0.586	0.649	0.898	1.347	0.796	0.880	1.186
3	0.433	0.654	0.653	0.523	0.764	0.775	0.372	0.586
4	0.410	0.671	0.689	0.625	0.879	0.658	0.633	0.619
5	0.414	0.771	0.707	0.566	0.900	0.665	0.399	0.612
6	0.455	0.588	0.674	1.275	1.212	1.666	0.544	0.770
7	0.414	0.609	0.682	0.751	1.247	0.754	0.465	1.162
8	1.406	0.531	0.678	0.846	0.927	0.919	0.472	0.787
Average	0.555	0.628	0.672	0.766	1.014	0.883	0.533	0.813

Using field observations to inform thermal hydrology models

A. L. Atchley et al.

Title Page

Abstract

Introduction

Conclusions

References

Tables

Figures



Back

Close

Full Screen / Esc

Printer-friendly Version

Interactive Discussion



Table 3. Measured snow depth ranges were gathered from a compilation of 258 snow depth measurements taken 2 May 2013 in the area encompassing all three borehole temperature measurements. Utm coordinates: Northing 7910330–7910350, Easting 585900–585930. Measured snow water equivalence (SWE) ranges were calculated from measured snow depth and the measured average snowpack density of 326 [kg m⁻³]. All simulated values were taken on simulation day 2 May 2013.

	Snow Depth [cm]		Snow Density [kg m ⁻³]		Snow Water Eqv. [cm]	
	Measured Range	Simulated	Measured Ave.	Simulated	Measured Range	Simulated
Center	20–40	24.6	326	349.3	6.5–13	9.5
Rim	10–20	14.6		320.2	3.25–6.5	5.2
Trough	40–60	40.3		370.4	13–19.5	16.25

Using field observations to inform thermal hydrology models

A. L. Atchley et al.

Table 4. The ALT for all three columns are listed for each iteration of the calibration process, also with the range of possible ALT from the observed data. The observed ALT range was made by finding the deepest borehole measurement for center rim and trough with a temperature above 0°C for at least a day and the shallowest borehole measurement with all temperatures below 0°C.

	Center	Rim	Trough
Calibrated Subsurface	48.2	44.2	48.1
Surface Energy Balance	37.7	41.0	33.7
Snow Distribution	40.5	41.3	38.4
Observed ALT	50–60	40–50	35–40

Title Page

Abstract

Introduction

Conclusions

References

Tables

Figures



Back

Close

Full Screen / Esc

Printer-friendly Version

Interactive Discussion



Using field observations to inform thermal hydrology models

A. L. Atchley et al.

Title Page

Abstract

Introduction

Conclusions

References

Tables

Figures

◀

▶

◀

▶

Back

Close

Full Screen / Esc

Printer-friendly Version

Interactive Discussion



Table 5. Final Calibrated Parameter Table (referred to throughout the text).

Notation/Units	Calibrated Moss	Calibrated Peat	Calibrated Mineral (Silty Loam)
Porosity [–]	0.9	0.876	0.596
VG Alpha [1 Pa^{-1}]	2.3×10^{-3}	9.5×10^{-4}	3.3×10^{-4}
VG n [–]	1.38	1.44	1.33
Residual VWC [–]	0.05	0.34	0.199
$K_{\text{dry,Bulk}}$ [$\text{W m}^{-1} \text{ K}^{-1}$]	0.024	0.025	0.104
$K_{\text{unfrozen,Bulk Sat}}$ [$\text{W m}^{-1} \text{ K}^{-1}$]	0.446	0.427	0.788
$K_{\text{frozen,Bulk Sat}}$ [$\text{W m}^{-1} \text{ K}^{-1}$]	1.81	1.73	3.2
$K_{\text{dry,material}}$ [$\text{W m}^{-1} \text{ K}^{-1}$]	0.1	0.11	2.23
$\alpha_{\text{T,uf}}$ [–]	0.5	0.4	0.8
$\alpha_{\text{T,f}}$ [–]	1	2	0.73

^a $K_{\text{dry,Bulk}}$, $K_{\text{frozen,Bulk}}$, and $K_{\text{unfrozen,Bulk}}$ [$\text{W m}^{-1} \text{ K}^{-1}$] are back calculated from $K_{\text{material,Bulk}}$.

Using field observations to inform thermal hydrology models

A. L. Atchley et al.

Title Page

Abstract

Introduction

Conclusions

References

Tables

Figures



Back

Close

Full Screen / Esc

Printer-friendly Version

Interactive Discussion



Table B1.

Surface	Albedo	Range
Ice ^a	0.44	0.27–0.49
Water ^b	0.141	0.112–0.202
Tundra ^a	0.135	0.12–0.17

^a From Grenfell and Perovich (2004).

^b From Cogley (1979).

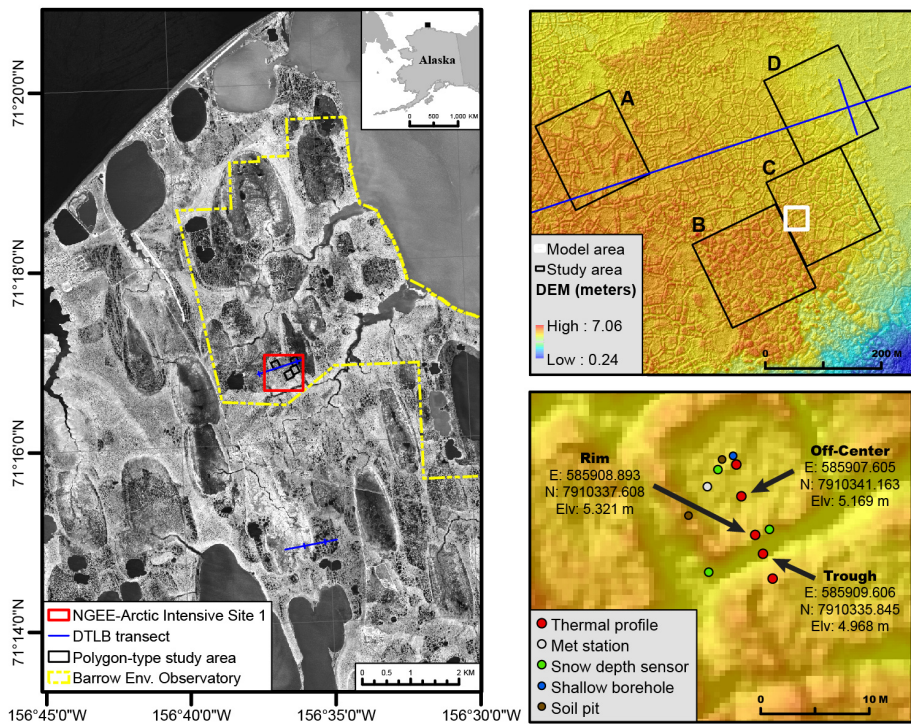


Figure 1. LIDAR of site-C with the three observation locations mapped and greater Barrow, AK area (Credit Garrett Altmann).

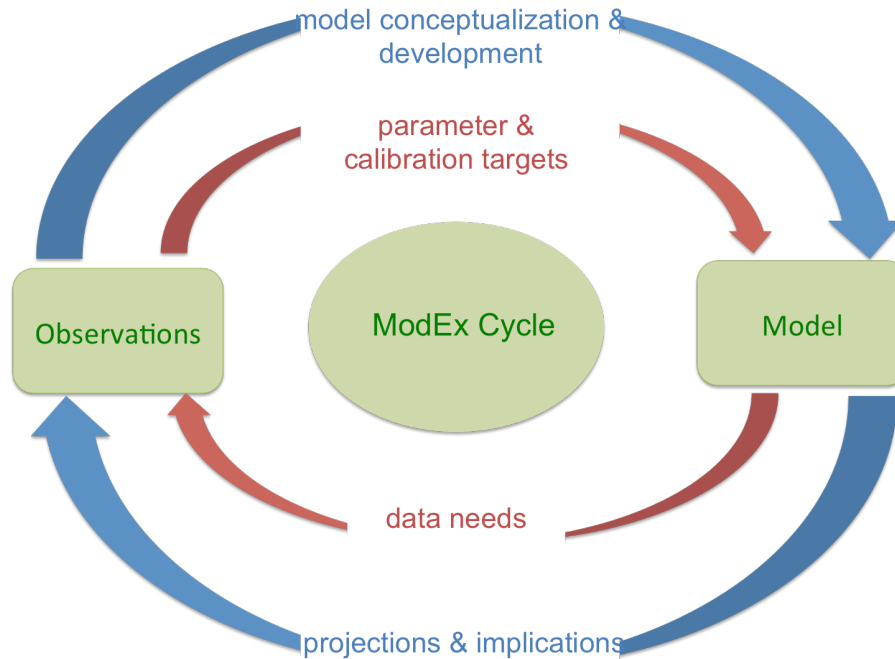


Figure 2. Schematic representation of a Model Observation/Experiment (ModEx) process involving traditional parameter estimation/calibration (inner loop) and model structural/conceptual refinement (outer loop). Observations inform simulation input and provide a starting point for a conceptual model. Both the conceptual and numerical model is then tested against observations. In successive ModEx iterations the model is then refined and at times re-drawn in order to elicit governing processes that shape model outcome to match observed and measured phenomena. Finally model experiments and the identification of governing processes inform future observations as to which measurements are needed to assess the state of the system.

Using field observations to inform thermal hydrology models

A. L. Atchley et al.

Title Page	
Abstract	Introduction
Conclusions	References
Tables	Figures
⏪	⏩
◀	▶
Back	Close
Full Screen / Esc	
Printer-friendly Version	
Interactive Discussion	



Using field observations to inform thermal hydrology models

A. L. Atchley et al.

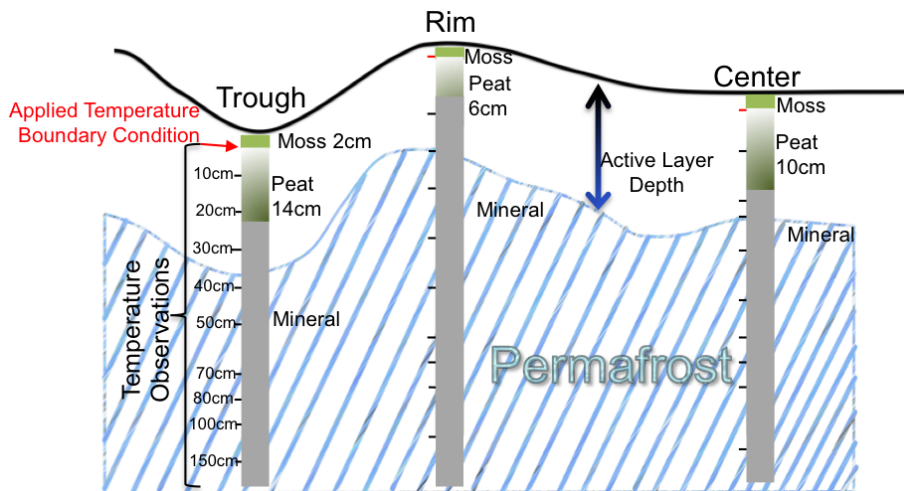


Figure 3. Diagram of the three 1-D columns and the associated measured soil temperature depths.

Title Page

Abstract

Introduction

Conclusions

References

Tables

Figures

⏪

⏩

◀

▶

Back

Close

Full Screen / Esc

Printer-friendly Version

Interactive Discussion



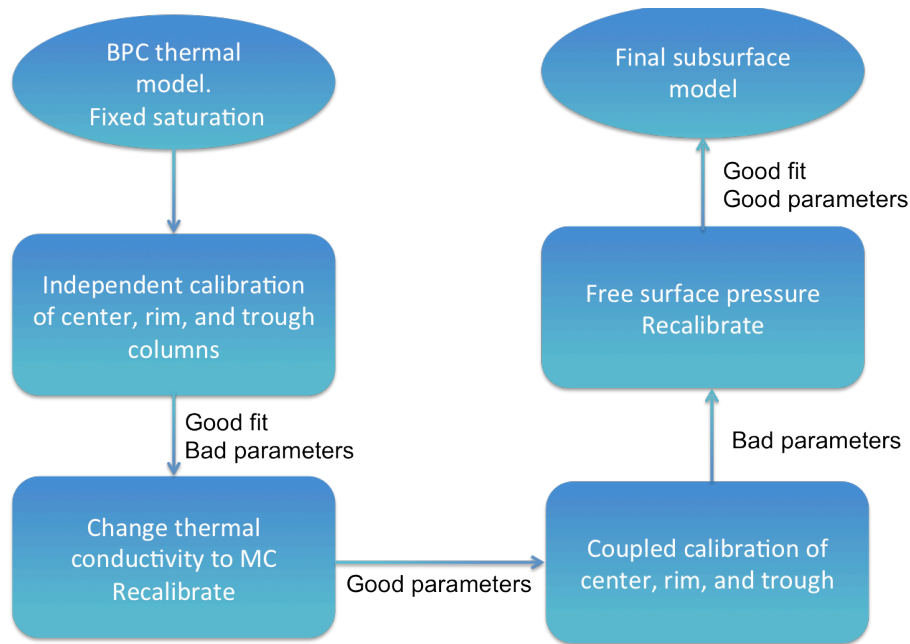


Figure 4. The ModEx cycle as applied here to subsurface thermal hydrologic system in freezing/thawing soils.

Using field observations to inform thermal hydrology models

A. L. Atchley et al.

[Title Page](#)

[Abstract](#) | [Introduction](#)

[Conclusions](#) | [References](#)

[Tables](#) | [Figures](#)

[◀](#) | [▶](#)

[◀](#) | [▶](#)

[Back](#) | [Close](#)

[Full Screen / Esc](#)

[Printer-friendly Version](#)

[Interactive Discussion](#)



Using field observations to inform thermal hydrology models

A. L. Atchley et al.

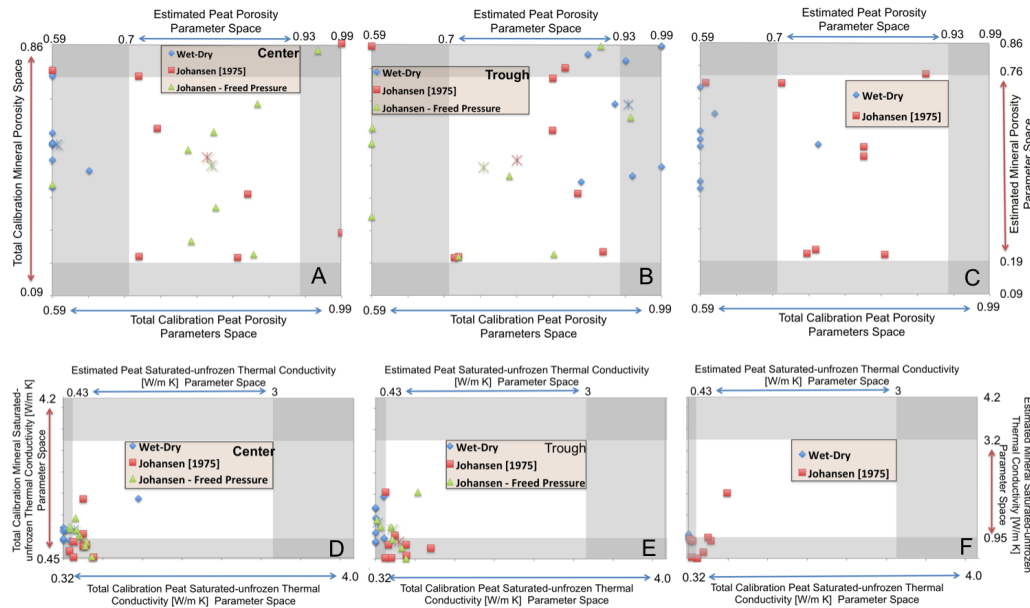


Figure 5. Plots A, B, and C show center, trough and rim respective calibrated peat and mineral porosities from 8 calibrations starts. Plots D, E, and F show calibrated saturated unfrozen thermal conductivities ($K_{\text{sat,uf}}$) for peat and mineral soil layers from the same 8 calibrations starts. $K_{\text{sat,uf}}$ values from the MC calibration are calculated from Eq. (3). Blue diamonds used the BPC model for soil thermal conductivity, red squares used the MC model for soil thermal conductivity, and green triangles added surface pressures as a free calibration parameter to the MC model for soil thermal conductivity. Color-coded asterisks represent the average calibrated parameter for each model tested for the 8 calibration starts, but are not actual calibrated results. Accepted parameter space delineated from literature and site observations in all cases are mapped as clear areas. Shaded areas are the calibration space outside of the acceptable parameter space. This figure shows how the calibration response surface changes as the model changed from (1) BPC to (2) MC to (3) unsaturated.

Title Page

Abstract Introduction

Conclusions References

Tables Figures

◀ ▶

◀ ▶

Back Close

Full Screen / Esc

Printer-friendly Version

Interactive Discussion



Using field observations to inform thermal hydrology models

A. L. Atchley et al.

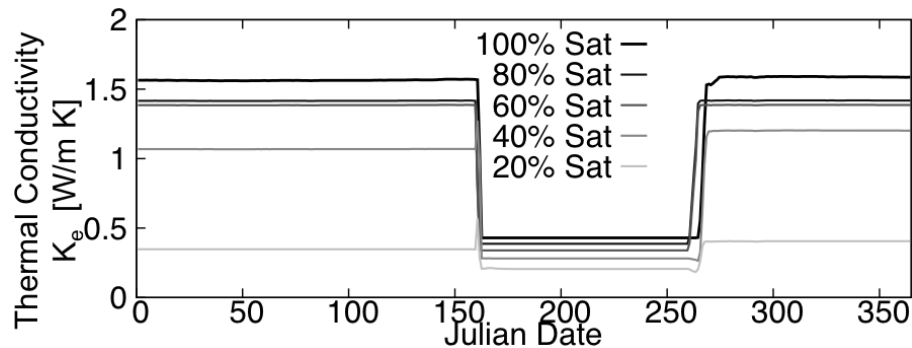


Figure 6. Thermal conductivity of peat throughout a year with different surface pressures. Percent liquid saturation is based off of summer time water liquid saturation, which changes during winter due to an increase in ice saturation. The change in thermal conductivity coincides with spring thaw, approximately Julian Day 160 or early-June, and fall freeze-up near Julian Day 265 or late September.

[Title Page](#)[Abstract](#)[Introduction](#)[Conclusions](#)[References](#)[Tables](#)[Figures](#)[◀](#)[▶](#)[◀](#)[▶](#)[Back](#)[Close](#)[Full Screen / Esc](#)[Printer-friendly Version](#)[Interactive Discussion](#)

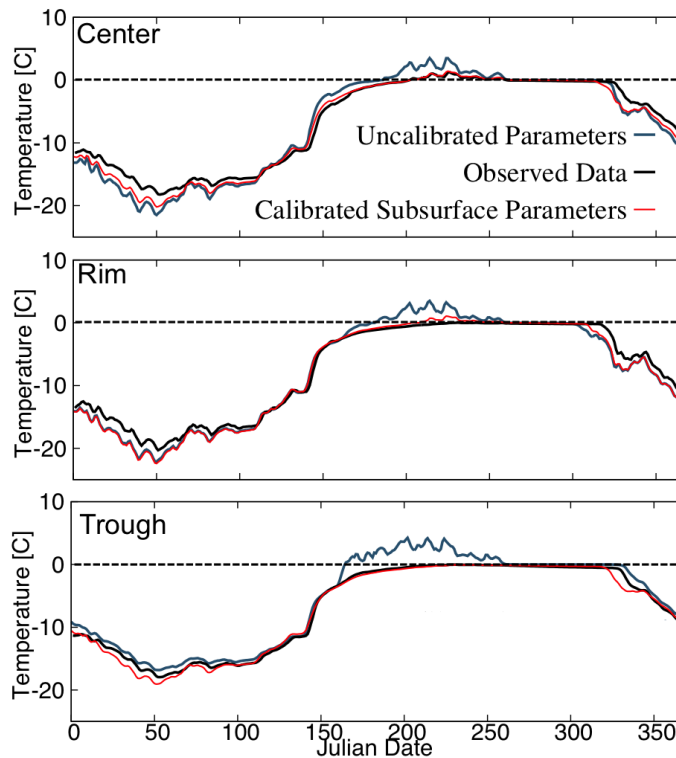


Figure 7. The subsurface un-calibrated and calibrated temperature time-series is compared to measured soil temperature time-series to showcase the improvement from the calibration process at 40 cm depth for the center, trough, and rim. The initial un-calibrated parameters were selected from the literature search described in Sect. 2.4 and Appendix C. Calibration fit to observation varies from the three columns, but shows marked improvement from initial un-calibrated time-series and are most accurate for all three during the summer at depth where active layer thickness is delineated.

Using field observations to inform thermal hydrology models

A. L. Atchley et al.

Title Page

Abstract	Introduction
Conclusions	References
Tables	Figures

⏪ ⏩
◀ ▶

Back	Close
------	-------

Full Screen / Esc

Printer-friendly Version

Interactive Discussion



Using field observations to inform thermal hydrology models

A. L. Atchley et al.

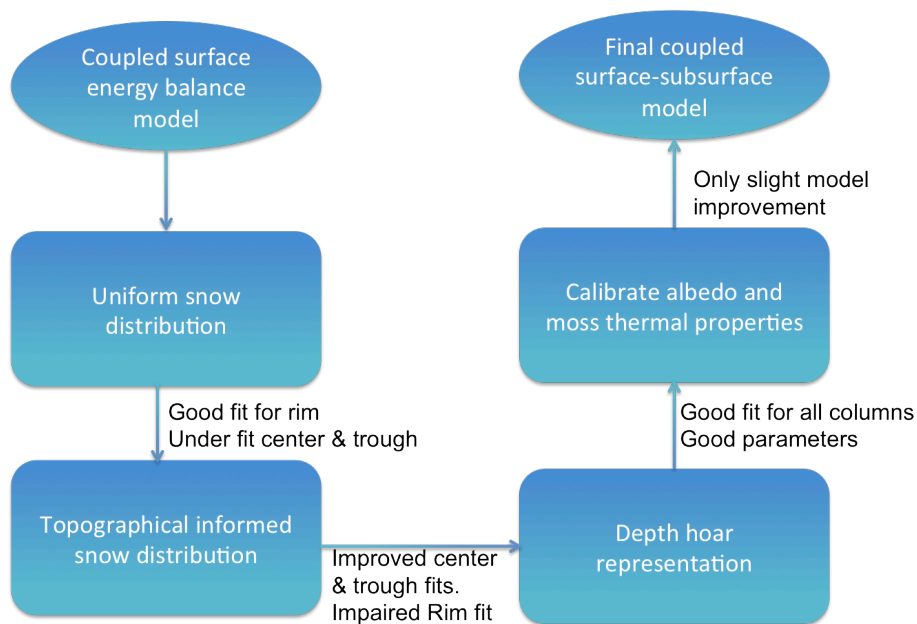


Figure 8. The ModEx cycle applied to the surface energy balance and moss parameters.

Title Page	
Abstract	Introduction
Conclusions	References
Tables	Figures
◀	▶
◀	▶
Back	Close
Full Screen / Esc	
Printer-friendly Version	
Interactive Discussion	



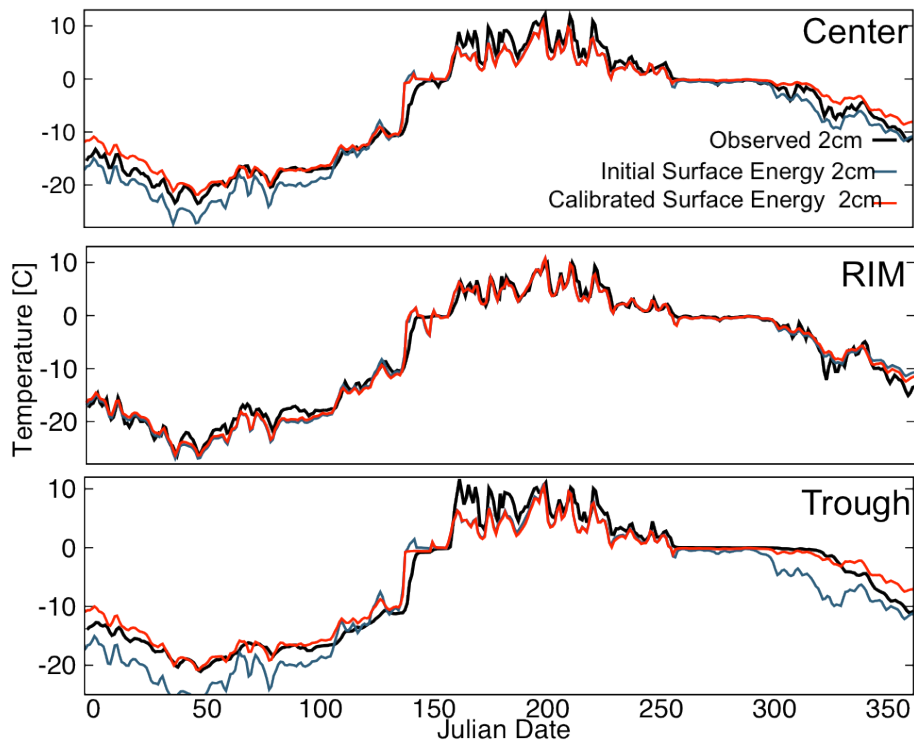


Figure 9. Soil temperature for a 2 cm depth are shown for the center (plot A), rim (plot B), and trough (plot C), using the initial surface energy balance parameters (blue), calibrated surface energy balance (red), and measured soil temperature (black). The biggest difference between initial temperature and the calibrated/observed is the wintertime temperature for each column and is a result of distributing snow on the center, rim, and trough and depth hoar representation. Snow distribution also had the greatest control in the ALT (Table 4).

Using field observations to inform thermal hydrology models

A. L. Atchley et al.

Title Page

Abstract Introduction

Conclusions References

Tables Figures

◀ ▶

◀ ▶

Back Close

Full Screen / Esc

Printer-friendly Version

Interactive Discussion



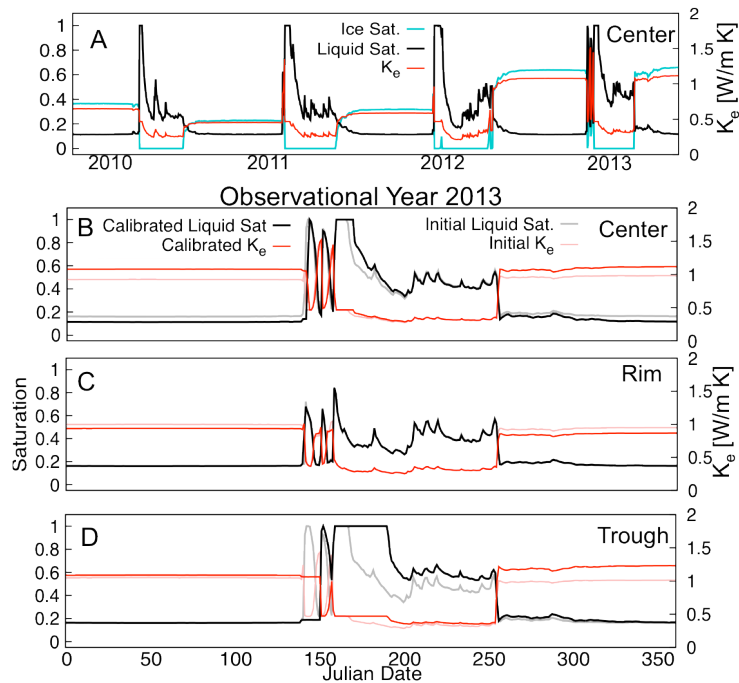


Figure 10. Ice and liquid saturation are shown in plot A for the simulated years of 2010–2013 at 2 cm depth along with bulk thermal conductivity for a center column. Notice that ice saturation and thermal conductivity during the winters are unique for each simulation year. Plots B, C, and D are zoomed in views of year 2013 of ice and liquid saturation and the bulk thermal conductivity for the center, rim, and trough respectively at a depth of 2 cm. Plots B–D have unique ice and liquid saturation and therefore bulk thermal conductivity for each column, which is a result of both the maximum ponded depth for each column and the snow distribution that mimics wind scouring of the snow surface at Barrow, AK.